JACS
JOURNAL OF THE AMERICAN CHEMICAL SOCIETY
pubs.acs.org/JACS
Article

A Mechanism-Based Strategy for Controlling CH_4 and CO Selectivities in CO_2−H_2 Reactions on Dispersed Ru, Co, and Ni Nanoparticles

Wenshuo Hu, Gregory L. Tate, and Enrique Iglesia*

Cite This: *J. Am. Chem. Soc.* 2025, 147, 19185−19199

Read Online

ACCESS | Metrics & More | Article Recommendations | Supporting Information

ABSTRACT: The formation of CO as an intermediate in the conversion of CO_2−H_2 to CH_4 and its strong binding on dispersed Ru, Co, and Ni nanoparticles inhibit rates of CO and CH_4 formation but to different extents. CO_2 conversion rates decrease and CH_4 selectivities increase as CO concentration gradients evolve axially along the catalyst bed and radially within diffusion-limited porous aggregates. These trends and their interpretation in terms of the identity and kinetic relevance of surface-catalyzed elementary steps enable mechanism-based strategies for selectivity control through the purposeful introduction of CO pressures into inlet CO_2−H_2 streams. This strategy exploits the stronger CO inhibition of its formation (from CO_2) than its conversion (to CH_4), which causes the selective inhibition of CO_2 conversion relative to CH_4 formation. The presence of CO at levels accurately prescribed by the mechanism-derived rate equations, similar in functional form on Ru, Co, and Ni nanoparticles, and by diffusion-convection-reaction models that account for CO gradients at the bed and aggregate scales led to the exclusive formation of CH_4 and to the elimination of CO gradients at both scales, as evident from measured rates and selectivities for CO_2−H_2 reactions on Ru, Co, and Ni nanoparticles over a broad and practical range of temperature (483−573 K), reactant pressures (4−1100 kPa CO_2; 8−820 kPa H_2), and nanoparticle diameter (2−30 nm). This mechanism-based strategy enables the exclusive formation of CH_4 from CO_2−H_2 reactants, irrespective of reaction conditions or nanoparticle composition (Ru, Co, Ni) and size, without requiring complex catalyst architectures or intricate synthesis protocols.

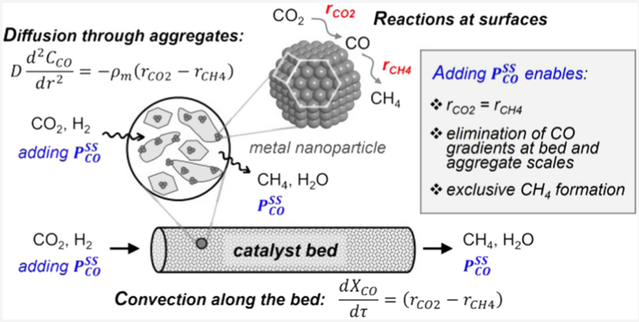

1. INTRODUCTION

Dispersed Ru,[1−4] Co,[5−7] and Ni[8−11] nanoparticles catalyze CO_2−H_2 reactions via the initial formation of CO and H_2O (reverse water−gas shift reaction, RWGS) and the sequential conversion of CO to CH_4 (methanation) and larger hydrocarbons (Fischer−Tropsch synthesis, FTS). RWGS and methanation reactions provide practical catalytic routes for converting CO_2 at moderate temperatures and pressures to marketable intermediates or products, as well as to molecules that can be used to store intermittent solar and wind sources as chemical energy.[2,3,7,12,13] The control of selectivity (CO vs. CH_4) in CO_2−H_2 reactions has focused on changes in the structure and composition of catalytic materials.[2,5,6,9,14−30] These efforts have included tailoring the size and composition of metal nanoparticles,[2,9,14−17] modifying their interactions with supports,[5,6,18−21] incorporating a second element in bimetallic nanoparticles,[22−26] or designing complex catalyst architectures, such as ordered porous structures or "single-atom" catalysts.[27−30] For instance, Ru nanoparticles dispersed on MoO_3 form defective MoO_{3-x} overlayers that decorate Ru surfaces,[18] leading to the proposal that such overlayers may selectively suppress methanation routes that require larger ensembles of contiguous surface Ru atoms than RWGS reactions.[3] Ni nanoparticles dispersed on hierarchically porous Co_3O_4 networks[30] and Ni−Pt bimetallic nanoparticles on mesoporous SiO_2 nanorods[23] led to the nearly exclusive formation of CH_4 from CO_2−H_2 reactants. ZrO_2 doped by "single-atoms" of Co instead converts CO_2 selectively to CO.[31]

These strategies require precise and often complex synthesis protocols, leading to ubiquitous hurdles in attempts to relate the structure of these solid catalysts to their specific function. Also, the requisite intricate inorganic structures proposed as the path to control selectivity are unlikely to persist during extended use under relevant conditions or after periodic regenerations. The present study demonstrates how mechanism-based considerations enable the exclusive formation of CH_4 through the purposeful control of CO concentration

Received: March 18, 2025
Revised: May 17, 2025
Accepted: May 20, 2025
Published: May 26, 2025

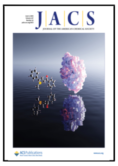

gradients at both bed and aggregate scales, irrespective of the composition (Ru, Co, Ni), the size or dispersion of the metal nanoparticles, or the reaction conditions (temperature, reactant pressures).

The conversion of CO_2-H_2 mixtures to CO and CH_4 on dispersed Ru, Co, and Ni nanoparticles involves sequential reactions of CO_2 to CO (and H_2O) and CO hydrogenation to CH_4.[3,5−11,16,32,33] CO forms via quasi-equilibrated CO_2 dissociation steps that form bound CO (CO*) and O* and subsequent kinetically-relevant steps that react O* species with H* to form OH*, with the OH* species ultimately forming H_2O via facile reactions with H*.[3,32] These mechanistic insights are consistent with the observed effects of CO_2, CO, and H_2 pressures on rates; they have been confirmed by fast isotopic scrambling of $C^{16}O_2-C^{18}O_2-H_2$ mixtures[3] and density functional theory (DFT) assessments of barriers and energies for elementary steps and intermediates on Ru nanoparticle models at high CO* coverages.[32] CO* species, present as nearly saturated dense adlayers in quasi-equilibrium with CO molecules in the fluid phase, then react with H* to form $[*HCO-H*]^{\ddagger}$ moieties as the kinetically-relevant transition state (TS) for CH_4 formation.[3,34−37] The proposed identity and reversibility of these steps lead to rate equations that accurately describe CO_2 conversion and CH_4 formation rates on dispersed Ru nanoparticles at all conditions examined.[3]

The sequential formation of CO and CH_4 from CO_2-H_2 reactants is also evident on dispersed Ni[8−11,16] and Co[5−7,33] nanoparticles. Infrared spectroscopy during catalysis and isotopic exchange data indicate that CO forms via direct CO_2 dissociation on Ni/SiO_2, while CH_4 forms via subsequent CO hydrogenation reactions.[9,16] Direct CO_2 dissociation to CO has been proposed as the predominant reaction channel for RWGS reactions on Co/TiO_2 catalysts,[33] instead of H-assisted routes that would initially form carbonate, formate, or formyl intermediates. CO molecules formed in these direct dissociation events then react with H_2 to form CH_4, either before desorption or after their desorption and readsorption along the bed.[33] These observations and mechanistic insights have confirmed the ubiquitous nature of gaseous and bound CO molecules, their presence as nearly saturated adlayers under practical conditions, and their intermediate role in the formation of CH_4 from CO_2-H_2 reactants.

CO* species formed via CO_2 dissociation are in quasi-equilibrium with CO (g) molecules in the contacting fluid phase during CO_2-H_2 reactions on Ru,[3,34,38] Co,[6,33,35] and Ni[9,11,16] nanoparticles. These dense CO* adlayers restrict the number and size of the ensembles of contiguous bare atoms required to stabilize the transition states that mediate the kinetically-relevant CO_2 and CO activation steps.[3,39,40] CO_2 conversion (r_{CO2}) and CH_4 formation (r_{CH4}) rates on these metals depend sensitively on CO pressure,[3,39] irrespective of whether CO is added with CO_2-H_2 reactants or formed indigenously from them. These inhibition effects render CO concentration gradients, both axially along the catalyst bed and radially within catalyst aggregates, consequential for measured r_{CO2} and r_{CH4} values and thus for CH_4 selectivities (defined as r_{CH4}/r_{CO2}). Such gradients must be considered in any kinetic analysis, as shown in previous studies that considered bed-scale CO gradients during CO_2-H_2 reactions on dispersed Ru nanoparticles using convection-reaction formalisms and plug-flow hydrodynamic constructs.[3]

This study exploits the consequences of these strong CO inhibition effects, which differ in magnitude for CO_2 conversion and CH_4 formation routes, to design and implement strategies to achieve the exclusive formation of CH_4 from CO_2-H_2 reactants on dispersed Ru, Co, and Ni nanoparticles. These strategies involve the purposeful addition of small amounts of CO to CO_2-H_2 reactants; the requisite inlet CO pressures are accurately predicted by mechanism-based rate equations for CO and CH_4 formation embedded within coupled diffusion-convection-reaction models. These strategies eliminate CO concentration gradients at both the catalyst bed and the porous aggregate scales by enforcing negligible net CO formation rates at each position along the bed and within the catalyst aggregates.

These strategies are broadly useful for CO_2-H_2 reactions on Ru, Co, and Ni nanoparticles over a wide range of temperatures (483−573 K), reactant pressures (4−1100 kPa CO_2; 8−820 kPa H_2), and nanoparticle diameters (2−30 nm). In practice, the small amounts of CO required to avoid any net CO formation can be readily recycled from effluent streams. This method enables any catalyst composition (Ru, Co, Ni) or nanoparticle structure under any reaction condition to form CH_4 exclusively, without requiring complex architectures or synthesis protocols; in doing so, these strategies replace the prevalent synthetic routes in our search for more active or selective catalysts for CO_2 conversion.

2. EXPERIMENTAL SECTION

2.1. Catalyst Synthesis and Characterization. Ru/SiO_2 (0.3%, 0.6%, and 1.2% wt) and Co/SiO_2 (20% wt) catalysts were prepared using incipient wetness impregnation methods. SiO_2 powders (Davisil 646 for Ru, 300 m^2 g^{-1}, 15 nm pore size; PQ Corp. CS-2133 for Co, 350 m^2 g^{-1}, 13 nm pore size) were impregnated with $Ru(NO)(NO_3)_3$ (1.5% wt Ru, Sigma-Aldrich) and $Co(NO_3)_2$ (Sigma-Aldrich) solutions, respectively, as described previously[3,34] (details in Supporting Information S1). Ni/SiO_2 (10% wt) was prepared by molten salt methods, with SiO_2 (Davisil 646, 300 m^2 g^{-1}; pore size: 15 nm) and $Ni(NO_3)_2$ (Sigma-Aldrich) mixed and treated in a rotary evaporator (Buchi R-210) at 353 K for 1 h (Section S1). These Ru-, Co-, and Ni-contained solids were then treated in flowing air, heated in flowing H_2, and passivated in flowing 1 kPa O_2 before exposure to ambient air, as detailed in Section S1.

The dispersion of metal (Ru, Co, Ni) nanoparticles, defined as the ratio of surface to total metal atoms (denoted as M), was measured by H_2 chemisorption by assuming a 1:1 $M_{surface}/H$ stoichiometry[3,34,41] (Section S1). Surface-averaged nanoparticle diameters ($\langle d_p \rangle$) were determined from dispersion values by assuming spherical crystallites and the bulk atom density of elements in their metallic state.

2.2. Measurements of CO_2-H_2 Reaction Rates and Selectivities. Kinetic measurements were performed in a fixed-bed metal reactor with a quartz liner (5 mm ID). The bed was heated using a three-zone resistively heated furnace, with temperatures set electronically (Watlow, EZ-ZONE PM Series) and measured by a K-type thermocouple inserted inside the quartz liner. The system pressure was set by a dome-loaded pressure regulator (Mity-Mite, stainless steel). Inlet molar flow rates of CO_2 (99.995%, Praxair), H_2 (99.999%, Praxair), CO (1% CO/He, Praxair), and He as the inert balance (99.999%, Praxair) were controlled electronically (Parker, 201). The composition of the effluent stream was measured by gas chromatography (Shimadzu GC-2014) using thermal conductivity for CO, CH_4, and CO_2 after separation by a packed column (Porapak Q, 3.7 m length, 2 mm ID) and flame ionization for detecting CH_4 and any other hydrocarbons (>93% CH_4, molar basis) after separation by a capillary column (HP-1, 25 m, 0.32 mm ID).

All catalyst samples were pressed, ground, and sieved (250−400 μm for 0.3% and 1.2% wt Ru/SiO_2, Ni/SiO_2, and Co/SiO_2; 149−177 and 1000−2000 μm for 0.6% wt Ru/SiO_2), and physically mixed with

SiO_2 (Davisil 646, 300 m^2 g^{-1}; pore size: 15 nm) for interparticle dilution. These mixtures were placed within the quartz liner and treated at 673 K (0.17 K s^{-1}; 773 K for Ni/SiO_2) for 1 h in flowing H_2 (100 kPa, 0.8 cm^3 s^{-1}) and then cooled to the target reaction temperature (483−573 K). All rates are reported as turnover rates (per exposed metal atom from H_2 uptakes; Section 2.1).

3. RESULTS AND DISCUSSION

3.1. Bed-Scale Axial CO Concentration Gradients and Consequences for CH_4 Selectivity on Ru-Based Catalysts. Scheme 1 depicts plausible elementary steps for CO_2−H_2 reactions on Ru nanoparticle surfaces densely covered by CO*; these steps include the formation of CO* (and O*) via quasi-equilibrated direct CO_2 dissociation, CO* desorption as CO (g) and its readsorption in quasi-equilibrated processes, and CO* coverages at near-saturation values.[3,32] CO_2 conversion turnovers are completed by subsequent kinetically-relevant steps of O* reactions with H* (in quasi-equilibrium with H_2 (g)) to form OH* (via the $[O-H]^‡$ TS), which then reacts with another H* in a facile step that forms the H_2O coproducts. CH_4 forms via hydrogenation of CO* through a kinetically-relevant $[^*HCO-H^*]^‡$ TS. These mechanistic details were elucidated through kinetic, spectroscopic, and isotopic measurements for Ru-based catalysts[3] and further supported by theoretical calculations assessing the stability of the proposed intermediates and transition states on Ru nanoparticle models at high CO* coverages.[32]

Scheme 1. Elementary Steps for CO_2−H_2 Reactions to CO and CH_4 on Dispersed Metal Nanoparticles[a]

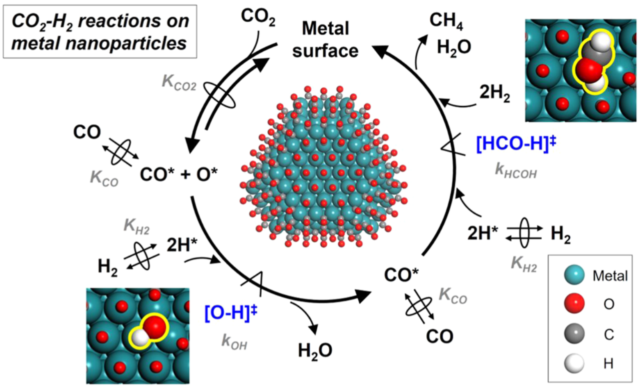

[a]Double arrows with superimposed ovals denote quasi-equilibrated steps (with equilibrium constants); arrows with conjunction operators denote kinetically-relevant steps (with rate constants), with their TS highlighted in blue. The center structure illustrates a metal nanoparticle with high CO* coverages; illustrative molecular structures for $[O-H]^‡$ and $[HCO-H]^‡$ are displayed with their boundary highlighted in yellow.

The elementary steps and reversibility assumptions described in Scheme 1 lead to specific functional forms for the equations that describe the rates of CO_2 conversion (r_{CO2}) and CH_4 formation (r_{CH4}) (detailed derivations in Section S2):[3,32]

$$r_{CO2} = \frac{\alpha P_{CO2}\sqrt{P_{H2}}}{P_{CO}(1 + \beta P_{CO} + \delta\sqrt{P_{H2}} + \sigma P_{CO2}\sqrt{P_{H2}})} \tag{1}$$

$$r_{CH4} = \frac{\gamma P_{CO}P_{H2}}{(1 + \beta P_{CO} + \delta\sqrt{P_{H2}} + \sigma P_{CO2}\sqrt{P_{H2}})^2} \tag{2}$$

Here, P_i (i = CO_2, H_2, CO) represents the pressure of species i, and α and γ are lumped rate parameters for the elementary steps involved in CO_2 conversion and CH_4 formation (Scheme 1), respectively. The β, δ, and σ parameters are the binding constants for the CO, H, and formate (or carboxylate) species, respectively; they determine their respective coverages on metal surfaces during steady-state catalysis. The β, δ, and σ parameters are explicitly included in rate equations (eqs 1 and 2) because the species to which they correspond have been detected spectroscopically (e.g., Ru/SiO_2,[3] Ru/TiO_2,[1,4] Co/Al_2O_3,[33] Ni/SiO_2[9,16]) or proposed as abundant bound species based on theoretical treatments (e.g., Ru(0001)[42] and Ni(111)[43]) at conditions relevant to CO_2−H_2 reactions. Their relative prevalence depends on the identity of the metal and on the temperature and pressure of their respective precursors under each condition; though unlikely to be present at detectable coverages for all conditions and catalysts, they are included here to maintain generality and completeness.

CO, formed as an intermediate product in CO_2−CO−CH_4 reactions, inhibits CO and CH_4 formation rates through competitive binding with other intermediates and transition states.[3,32] These CO* species decrease the number and size of the ensembles of bare surface atoms required to stabilize the kinetically-relevant TS structures for CO_2 conversion and CH_4 formation. These CO inhibition effects are evident from the βP_{CO} terms in eqs 1 and 2, which cause r_{CO2} (eq 1) and r_{CH4} (eq 2) to decrease as CO forms along the catalyst bed. Consequently, differential kinetic formalisms, which assume rates to remain constant along the bed, are inappropriate for assessing the merits of any mechanism-based rate equations.

Convection-reaction models account for bed-scale axial CO gradients and for their consequences for CO_2 conversion and CH_4 formation rates.[3] These formalisms require the simultaneous regression of rate data for CO_2 conversion and CH_4 formation to coupled differential mole balances that prescribe how CO pressures evolve along the bed based on the relative rates of CO formation (eq 1) and consumption (eq 2) via the sequential reactions in Scheme 1:

$$\frac{dX_{CO2}}{d\tau} = r_{CO2}\cdot(1 - \eta_{RWGS}) \tag{3}$$

$$\frac{d\psi_{CH4}}{d\tau} = r_{CH4} \tag{4}$$

Here, τ is the bed residence time (defined as the ratio of surface metal atoms to inlet CO_2 molar rates), X_{CO_2} is the fractional CO_2 conversion, and ψ_{CH4} is the ratio of CH_4 molar rates at each axial position to the CO_2 molar rates at the bed inlet. The η_{RWGS} term accounts for the approach to equilibrium for the conversion of CO_2 to CO via RWGS:

$$\eta_{RWGS} = \frac{P_{CO}P_{H2O}}{P_{CO2}P_{H2}}\cdot\frac{1}{K_{RWGS}} \tag{5}$$

with K_{RWGS} as the RWGS equilibrium constant. CO_2 conversion to CH_4 and H_2O remains far from equilibrium (η < 0.01) for all experiments reported in this study, thus requiring no thermodynamic corrections. Such corrections can be included by multiplying r_{CH4} by a $(1 - \eta_{CH4})$ term in eq 4, when warranted by the different ranges of conditions encountered in practice.

These convection-reaction mole balances (eqs 3 and 4) use mechanism-based rate equations for CO formation and

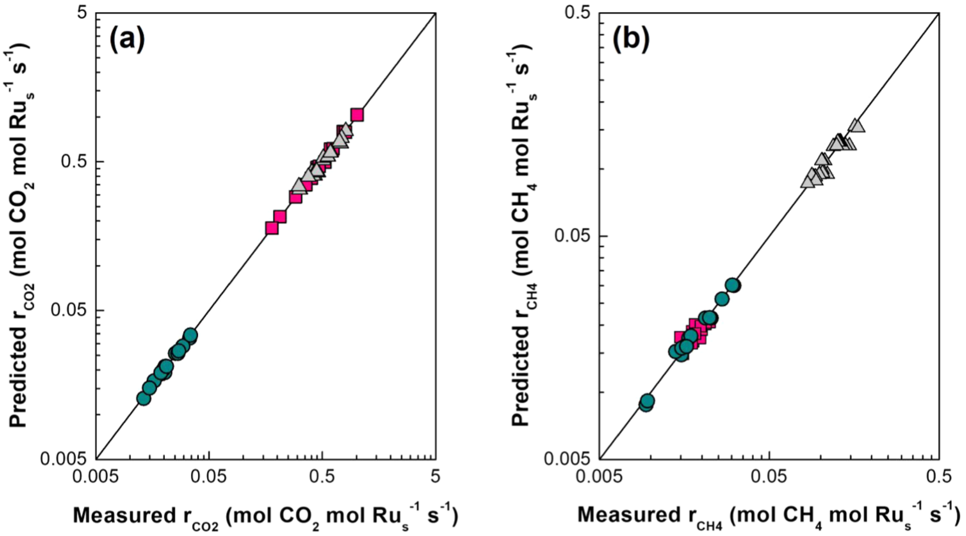

Figure 1. Measured and predicted (eqs 3 and 4 with eqs 1 and 2) (a) CO_2 conversion and (b) CH_4 formation rates on 0.3% wt Ru/SiO_2 (triangles; $\langle d_p \rangle$=11 nm; 5−85 kPa CO_2, 9−13 kPa H_2, 573 K), 1.2% wt Ru/SiO_2 (circles; 3 nm; 140−640 kPa CO_2, 64−320 kPa H_2, 483 K), and 0.6% wt Ru/SiO_2 (squares; 2 nm; 4−32 kPa CO_2, 8 kPa H_2, 573 K; aggregate radius: 82 μm).

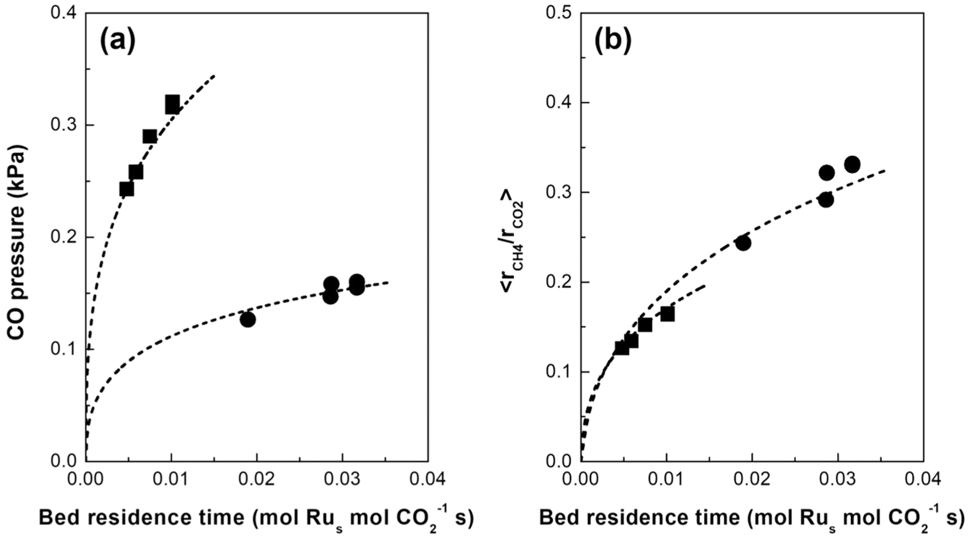

Figure 2. Measured (a) CO pressures and (b) CH_4 selectivities at different bed residence times for CO_2−H_2 reactions on 0.3% wt Ru/SiO_2 ($\langle d_p \rangle$=11 nm; 573 K; circles: 18 kPa CO_2, 12 kPa H_2; squares: 68 kPa CO_2, 10 kPa H_2). Dashed curves are regression results from the convection-reaction model (eqs 3 and 4) using rate equations eqs 6 and 7.

consumption (eqs 1 and 2) to describe the measured rates of CO_2 conversion and CH_4 formation on SiO_2-supported Ru nanoparticles spanning a range of mean diameter ($\langle d_p \rangle$, 2−11 nm) and relevant ranges of temperature (483−573 K) and reactant pressures (4−640 kPa CO_2, 8−320 kPa H_2). The accurate descriptions (parity plots, Figure 1) indicate that reaction rates across these broad ranges of nanoparticle size, temperature, and CO_2 and H_2 pressures are determined by the identity and kinetic relevance of the elementary steps (Scheme 1) that mediate these reactions and from which the functional forms of eqs 1 and 2 arise.

Reaction temperatures and pressures of CO_2 and H_2 reactants influence the relative coverages of bound species on Ru surfaces because they determine the prevalent CO pressure and the rates of formation and consumption of different intermediates. Ru catalysts ($\langle d_p \rangle$, 2 and 11 nm) at higher temperatures (573 K) and lower CO_2−H_2 pressures (4−85 kPa CO_2, 8−13 kPa H_2) showed undetectable H* and formate (or carboxylate) fractional coverages (<0.01, calculation details in Section S2) and surfaces that become predominantly covered by CO* and detectable, but lower coverages of bare sites (*). These inferences are consistent with infrared spectra at similar conditions (5−25 kPa CO_2, 8 kPa H_2, 573 K) for Ru/SiO_2 catalysts ($\langle d_p \rangle$=6 nm), which showed the predominant presence of CO* at near-saturation coverages.[3] At such high CO* coverages, CO formation and consumption rates (eqs 1 and 2) become:

$$r_{CO2} = \frac{\alpha P_{CO2}\sqrt{P_{H2}}}{P_{CO}(1 + \beta P_{CO})} \tag{6}$$

$$r_{CH4} = \frac{\gamma P_{CO} P_{H2}}{(1 + \beta P_{CO})^2} \tag{7}$$

Table 1. Regressed Rate Parameters for CO_2 Conversion (Eqs 6 and 12) and CH_4 Formation (Eqs 7 and 13) on Ru/SiO_2 Catalysts

catalyst	mean nanoparticle diameter (nm)	temperature (K)	α ($kPa^{-0.5}$ s^{-1})	β (kPa^{-1})	γ (kPa^{-2} s^{-1})
Ru/SiO_2 (0.3% wt)	11	573	2.9 (±0.5) × 10^{-3}[a]	29 (±8)	2.1 (±0.9)
Ru/SiO_2 (0.6% wt)	2	573	2.7 (±1.0) × 10^{-3}	22 (±6)	0.24 (±0.09)
Ru/SiO_2 (1.2% wt)	3	483	α/β ($kPa^{0.5}$ s^{-1})	δ/β ($kPa^{0.5}$)	γ/β^2 (s^{-1})
			1.3 (±0.1) × 10^{-6}	0.02 (±0.002)	1.4 (±0.1) × 10^{-4}

[a] Uncertainties represent 95% confidence intervals.

Equations 6 and 7 represent the asymptotic forms of eqs 1 and 2 for surfaces predominantly covered by CO* and bare sites, with the two denominator terms (βP_{CO} and unity) accounting for their respective relative abundance.

The intermediate role of CO in the CO_2−CO−CH_4 reaction sequences leads to *net* CO formation rates given by the differences between its formation and consumption rates at each axial position (eq 8). The ψ_{CO} term stands for the ratio of the CO pressure at each axial position to the inlet pressure of CO_2. The right-hand side of eq 8 represents a mathematical “kernel” that determines the net rate of CO formation and thus the axial evolution in CO concentration; positive (or negative) kernels lead to an increase (or decrease) in CO pressures along the bed. Figure 2a shows these CO pressures at different bed residence times (τ, equivalent to axial position; 0.3% wt Ru/SiO_2; $\langle d_p \rangle$ = 11 nm) at two CO_2−H_2 reactant pressures (CO_2/H_2 = 18/12 and 68/10, kPa; 573 K; η_{RWGS} < 0.02) as an illustrative example. CO pressures increase with residence time, a trend accurately captured (dashed traces, Figure 2a) by the convection-reaction mole balances (eqs 3 and 4) with the asymptotic form of the rate equations (eqs 6 and 7; regressed parameters, Table 1) for conditions that lead to surfaces predominantly covered by CO* and bare sites, as in the case of the low CO_2 and H_2 pressures (18−68 kPa CO_2, 10−12 kPa H_2) and high temperature (573 K) used for the data shown in Figure 2.

$$\frac{d\psi_{CO}}{d\tau} = r_{CO2}\cdot(1 - \eta_{RWGS}) - r_{CH4} \tag{8}$$

The βP_{CO} term in eqs 6 and 7 accounts for the CO inhibition effects, as also evident by rearranging eq 6:

$$\frac{r_{CO2}}{P_{CO2}\sqrt{P_{H2}}} = \frac{\alpha}{P_{CO}(1 + \beta P_{CO})} \tag{9}$$

which renders the term on the left-hand side a single-valued function of P_{CO}. Figure 3 shows $r_{CO2}/(P_{CO2}\sqrt{P_{H2}})$ values at different mean CO pressures along the bed ($\langle P_{CO} \rangle$) for two Ru/SiO_2 catalysts with different nanoparticle sizes ($\langle d_p \rangle$, 11 and 2 nm) at similar reaction conditions (573 K; 11 nm: 17−85 kPa CO_2, 9−13 kPa H_2; 2 nm: 4−32 kPa CO_2, 8 kPa H_2). These $r_{CO2}/(P_{CO2}\sqrt{P_{H2}})$ ratios decreased monotonically with increasing $\langle P_{CO} \rangle$ values (Figure 3), but they did not show any additional dependence on the CO_2 or H_2 pressure, consistent with the functional form of eq 9.

The CH_4 selectivity measured at the reactor outlet is determined by the ratio of the cumulative amounts of CH_4 formed and CO_2 converted across the bed. Measured CH_4 selectivities increased with increasing bed residence time (τ; Figure 2b), a trend that is accurately described by the convection-reaction mole balances (eqs 3 and 4) using the asymptotic form of the rate equations (eqs 6 and 7; dashed curves, Figure 2b) and their regressed parameter values (0.3% wt Ru/SiO_2; Table 1). These selectivity trends reflect the monotonic increase in CO partial pressure along the bed (Figure 2a), together with CO inhibition effects that are stronger for CO_2 conversion (eq 6) than CH_4 formation (eq 7). These different CO inhibition effects cause r_{CO2} values to decrease more strongly than r_{CH4} values as CO forms along the bed, leading to higher CH_4 selectivities at the higher CO pressures that prevail at longer bed residence times (Figure 2b).

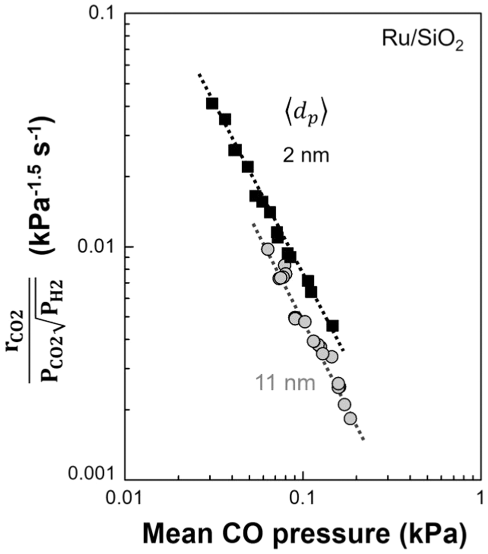

Figure 3. Measured $r_{CO2}/(P_{CO2}\sqrt{P_{H2}})$ (eq 9) values at different mean CO pressures on 0.3% wt Ru/SiO_2 ($\langle d_p \rangle$=11 nm; 573 K; 17−85 kPa CO_2, 9−13 kPa H_2) and 0.6% wt Ru/SiO_2 (2 nm; 573 K; 4−32 kPa CO_2, 8 kPa H_2; aggregate radius: 82 μm). Dashed lines denote the trend.

The axial profiles in CO pressure (Figure 2a) and CH_4 selectivity (Figure 2b) reflect the combined (net) effects of changes in the rates of CO formation (eq 6) and consumption (eq 7). These CO gradients can be used to control selectivity by exploiting the strong (but different) inhibition effects of CO on r_{CO2} and r_{CH4}, which, taken together, determine the net CO formation rates reflected in the “kernel” shown in eq 8 and thus CH_4 selectivities, as discussed next.

3.2. CO Addition Strategies for the Exclusive Formation of CH_4 from CO_2−H_2 Reactants.

The strategy of purposeful addition of CO to inlet streams, exploiting the different inhibition effects of CO on its formation and consumption to control CH_4 selectivity, is illustrated first for Ru catalysts at a specific temperature (573 K) and low reactant pressures (4−32 kPa CO_2, 8−12 kPa H_2), and then generalized to Ru, Co, and Ni nanoparticles over much broader and practical ranges of temperature (483−573 K) and reactant pressures (100−1100 kPa CO_2, 64−820 kPa H_2).

https://doi.org/10.1021/jacs.5c04698
J. Am. Chem. Soc. 2025, 147, 19185−19199

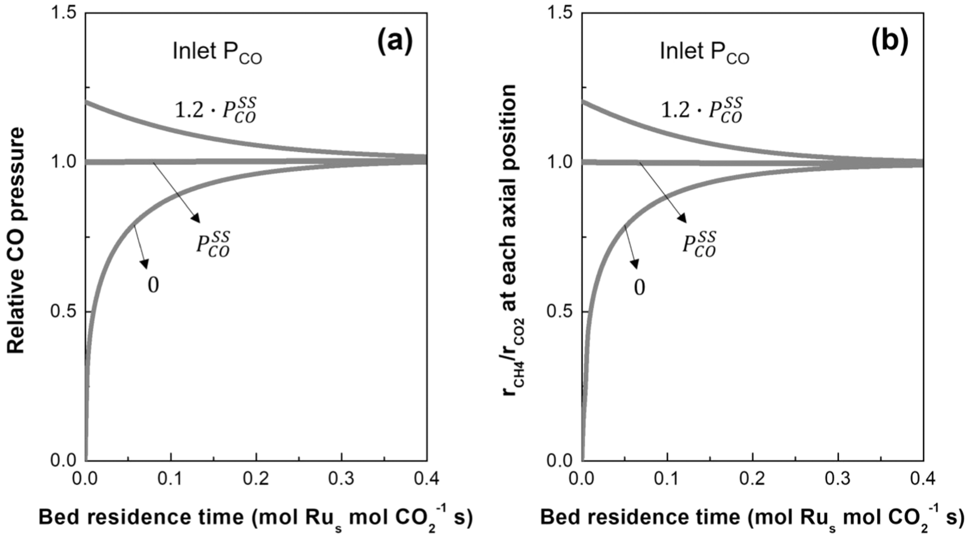

Figure 4. Axial evolution of (a) CO pressure and (b) local r_{CH4}/r_{CO2} ratio (eq 10) along the bed derived from the convection-reaction model (eqs 3 and 4) using asymptotic rate equations (eqs 6 and 7) and regressed parameters for 0.3% wt Ru/SiO$_2$ (Table 1; 18 kPa CO$_2$, 12 kPa H$_2$; 573 K; $\eta_{RWGS} < 0.1$) with different amounts of CO (0, P_{CO}^{SS}, 1.2P_{CO}^{SS}) added to the inlet CO$_2$−H$_2$ reactant streams.

3.2.1. CO Addition Strategies on Ru-Based Catalysts.

Figure 4 shows the CO pressures (P_{CO}; Figure 4a) and local r_{CH4}/r_{CO2} ratios (Figure 4b) at each axial position derived from the bed-scale convection-reaction mole balances (eqs 3 and 4) with rates given by eqs 6 and 7 (on 0.3% wt Ru/SiO$_2$, $\langle d_p \rangle$=11 nm, as the illustrative example). These simulations use the same CO$_2$ and H$_2$ pressures (18 kPa CO$_2$, 12 kPa H$_2$; 573 K; $\eta_{RWGS} < 0.1$) and rate parameters (Table 1) as those used to obtain the data shown in Figure 2, but with a 10-fold longer bed residence time (0.4 mol Ru$_s$ mol CO$_2^{-1}$ s, Figure 4) and different amounts of CO added to the CO$_2$−H$_2$ reactants at the inlet (0, P_{CO}^{SS}, 1.2 times P_{CO}^{SS}; P_{CO}^{SS} denotes the CO pressure at the bed outlet). The P$_{CO}$ values reported in Figure 4 were normalized by P_{CO}^{SS}, the steady-state CO pressure reached at sufficiently long bed residence times for any value of the inlet CO pressure. The high CO* coverages at Ru nanoparticle surfaces ($\beta P_{CO} \gg 1$), evident from infrared spectra during CO$_2$−H$_2$ reactions at similar pressures and temperatures (5−25 kPa CO$_2$, 8 kPa H$_2$, 573 K),[3] lead to r_{CH4}/r_{CO2} ratios at each axial position given by

$$\frac{r_{CH4}}{r_{CO2}} = \frac{\gamma}{\alpha\beta} \cdot \frac{P_{CO}\sqrt{P_{H2}}}{P_{CO2}} \tag{10}$$

This expression is derived from the asymptotic forms of eqs 6 and 7 for surfaces predominantly covered by CO*. The lumped parameter $\gamma/(\alpha\beta)$ depends on the properties of Ru nanoparticles at a given temperature;[3] it represents an intrinsic measure of CH$_4$ selectivity for CO$_2$−H$_2$ reactions on Ru nanoparticles of a given diameter and nearly saturated with CO*.[3] This lumped $\gamma/(\alpha\beta)$ parameter does not depend on CO$_2$, H$_2$, or CO pressures.

CO pressures (Figure 4a) and r_{CH4}/r_{CO2} ratios (Figure 4b) from bed-scale mole balances increase monotonically along the bed when CO is not present at the inlet (inlet P_{CO} = 0); they ultimately reach constant asymptotic values (P_{CO}^{SS} for the CO pressure and unity for r_{CH4}/r_{CO2}) at long bed residence times, consistent with negligible CO formation rates at any later axial bed positions. These trends reflect the stronger CO inhibition effects on CO$_2$ conversion (eq 6) than CH$_4$ formation (eq 7) and the concurrent (but different) decrease in both r_{CO2} and r_{CH4} as CO concentrations increase axially along the bed. CH$_4$ selectivities increase as conversion proceeds and CO pressures increase; the "kernel" in eq 8 (the net CO formation rate) ultimately becomes zero at some point along the bed, leading to the exclusive formation of CH$_4$ at any later axial positions. Such steady-state P_{CO} values (P_{CO}^{SS}) can be estimated by setting r_{CO2} (eq 6) and r_{CH4} (eq 7) equal to each other for any given inlet CO$_2$ and H$_2$ pressures, with the $\gamma/(\alpha\beta)$ value for a specific catalyst at a given temperature (and for conditions far from equilibrium; $\eta_{RWGS} \ll 1$):

$$P_{CO}^{SS} = \frac{\alpha\beta}{\gamma} \cdot \frac{P_{CO2}}{\sqrt{P_{H2}}} \tag{11}$$

This equation gives asymptotic P_{CO}^{SS} values specifically for reaction conditions leading to CO* at near-saturation coverages ($\beta P_{CO} \gg 1$ in eqs 6 and 7).

Figure 4 also shows the predicted CO pressures and r_{CH4}/r_{CO2} ratios at each axial position when CO is present along with CO$_2$−H$_2$ reactants in the inlet stream (18 kPa CO$_2$, 12 kPa H$_2$; 573 K; $\eta_{RWGS} < 0.1$) at a pressure corresponding to 1.2 times the steady-state P_{CO} value (1.2 P_{CO}^{SS}). Inlet CO pressures above P_{CO}^{SS} lead to r_{CH4}/r_{CO2} ratios (eq 10) larger than unity near the bed inlet (Figure 4b); this reflects the net consumption of CO (Figure 4a), a negative value of the "kernel" in eq 8, and a monotonic decrease in P_{CO} along the bed up to the point where it reaches the P_{CO}^{SS} value (Figure 4a) and r_{CH4}/r_{CO2} ratios become unity (Figure 4b). These asymptotic P_{CO}^{SS} values depend on the inlet CO$_2$ and H$_2$ pressures, but not on the inlet P_{CO} value, as the form of eq 11 shows.

The CO pressure can be kept constant throughout the bed simply by setting the inlet CO pressure at its P_{CO}^{SS} value. This avoids any net CO formation at any point along the bed (Figure 4a), eliminates axial CO concentration gradients, and causes the exclusive formation of CH$_4$ from CO$_2$−H$_2$ reactants (Figure 4b), irrespective of the intrinsic selectivity ($\gamma/(\alpha\beta)$, eq 10) of any specific catalyst. The $\gamma/(\alpha\beta)$ value sets, however, the required P_{CO}^{SS} value. In practice, maintaining such inlet CO levels merely requires the recycling of a small amount of CO from effluent streams. This provides a practical strategy for the exclusive formation of CH_4, irrespective of catalyst properties (e.g., intrinsic selectivity), reaction conditions (temperature, CO_2-H_2 pressures), or, as shown below, the diameter and elemental composition of the dispersed nanoparticles.

3.2.2. CO Addition Strategies: Experimental Validation. The predictions from the convection-reaction theoretical constructs and the success and general usefulness of these CO addition strategies (Figure 4) were confirmed experimentally from measured outlet CO pressures at different P_{CO2} and P_{H2} values (4−32 kPa of CO_2, 8 kPa of H_2; 573 K; $\eta_{RWGS} \leq 0.02$) and inlet CO pressures (P_{CO}^{SS}) predicted from eq 11 using the regressed parameters for 0.6% wt Ru/SiO_2 ($\langle d_p \rangle$ = 2 nm, Table 1). Bed residence times were chosen to ensure that P_{CO}^{SS} levels were reached at the bed outlet (eqs 3 and 4 with eqs 6 and 7 as the rate equations). Measured outlet CO pressures (squares, Figure 5) are similar to those added at the inlet and agree well with the P_{CO}^{SS} values predicted from eq 11, indicating that only CH_4 (and H_2O) was formed in CO_2-H_2 reactions. These data show that the presence of CO at the predicted P_{CO}^{SS} value in the inlet stream eliminates axial CO gradients and leads to the exclusive formation of CH_4 from CO_2-H_2 reactants, thus confirming the appropriateness and accuracy of the convection-reaction model and of the regressed kinetic parameters, as well as the reliability of CO addition as a general strategy for selectivity control.

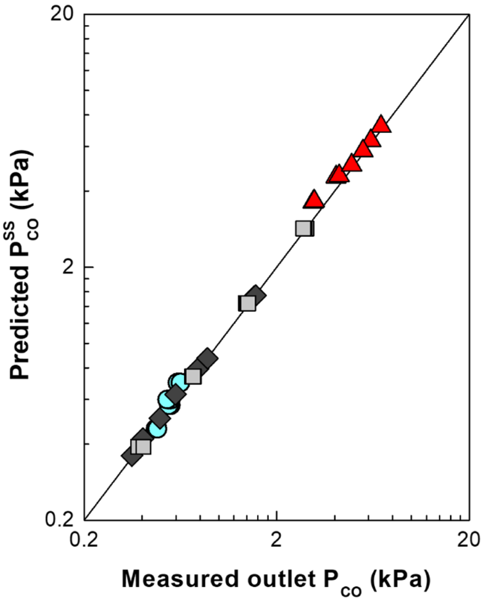

Figure 5. Measured outlet P_{CO} and predicted P_{CO}^{SS} values. Circles: 1.2% wt Ru/SiO_2 ($\langle d_p \rangle$=3 nm; 510−630 kPa CO_2, 64−320 kPa H_2; 483 K). Squares: 0.6% wt Ru/SiO_2 (2 nm; 4−32 kPa CO_2, 8 kPa H_2; 573 K; aggregate radius: 750 μm). Diamonds: 20% wt Co/SiO_2 (29 nm; 100−1100 kPa CO_2, 300−420 kPa H_2; 483 K). Triangles: 10% wt Ni/SiO_2 (8 nm; 200−440 kPa CO_2, 320−820 kPa H_2; 573 K).

These mechanistically-inspired CO addition strategies were also examined on Ru nanoparticles with larger diameters ($\langle d_p \rangle$ = 3 nm; 1.2% wt) at lower temperatures (483 K) and much higher reactant pressures (510−630 kPa CO_2, 64−320 kPa H_2). These low temperatures and high CO_2-H_2 pressures lead to Ru surfaces that are nearly saturated with a mixture of CO* and H* (instead of only CO*; fractional coverages of bare sites and formate/carboxylate species <0.1, Section S2) and to slightly more complex (compared with eqs 6 and 7) asymptotic forms of rate equations:

$$r_{CO2} = \frac{\frac{\alpha}{\beta} P_{CO2}\sqrt{P_{H2}}}{P_{CO}\left(P_{CO} + \frac{\delta}{\beta}\sqrt{P_{H2}}\right)} \tag{12}$$

$$r_{CH4} = \frac{\frac{\gamma}{\beta^2} P_{CO} P_{H2}}{\left(P_{CO} + \frac{\delta}{\beta}\sqrt{P_{H2}}\right)^2} \tag{13}$$

These equations, when embedded within the convection-reaction mole balances (eqs 3 and 4), accurately describe the r_{CO2} and r_{CH4} values measured on 1.2% wt Ru/SiO_2 ($\langle d_p \rangle$ = 3 nm; 140−640 kPa CO_2, 64−320 kPa H_2, 483 K; parity plots, Figure S1; regressed parameters, Table 1).

The P_{CO}^{SS} values obtained by equating r_{CO2} (eq 12) and r_{CH4} (eq 13) at each CO_2 and H_2 inlet pressures are given by

$$P_{CO}^{SS} = \frac{\alpha\beta}{\gamma}\cdot\frac{P_{CO2}}{\sqrt{P_{H2}}}\cdot\left(\frac{1}{2} + \sqrt{\frac{1}{4} + \frac{\gamma\delta}{\alpha\beta^2}\cdot\frac{P_{H2}}{P_{CO2}}}\right) \tag{14}$$

This expression reduces to eq 11 when H* coverages are much lower than for CO* ($\frac{\gamma\delta}{\alpha\beta^2}\cdot\frac{P_{H2}}{P_{CO2}} \ll \frac{1}{4}$, eq 14). The outlet CO pressures were measured at different inlet P_{CO2} and P_{H2} values (P_{CO2}/P_{H2} = 630/200, 516/128, 516/64, and 510/320 kPa), in each case with three different inlet CO additions (0, P_{CO}^{SS}, and 1.1 P_{CO}^{SS}). Measured outlet CO pressures agree well with the P_{CO}^{SS} values (circles, Figure 5) predicted from eq 14 using the regressed parameters for 1.2% wt Ru/SiO_2 (483 K, Table 1). These outlet CO pressures depend on the inlet P_{CO2} and P_{H2} values, but not on inlet CO pressures, in line with the functional form of eq 14. These data, together with those for 0.6% wt Ru/SiO_2 (squares, Figure 5) at higher temperatures (573 K) and much lower reactant pressures (4−32 kPa CO_2, 8 kPa H_2), confirm the general usefulness of the CO addition strategy for selectivity control across a broad range of temperature (483−573 K) and pressure (4−630 kPa CO_2, 8−320 kPa H_2).

The predicted P_{CO}^{SS} values depend on the magnitude of the lumped $\gamma/(\alpha\beta)$ parameter (eqs 11 and 14); this parameter

Table 2. Mean Nanoparticle Diameters, Reaction Conditions, and Intrinsic Selectivity Parameters for Catalysts Shown in Figure 5

catalyst	mean nanoparticle diameter (nm)	temperature (K)	CO_2 pressure (kPa)	H_2 pressure (kPa)	$\gamma/(\alpha\beta)^{a}$ ($kPa^{-0.5}$)
Ru/SiO_2 (0.6% wt)	2	573	4−32	8	4
Ru/SiO_2 (1.2% wt)	3	483	510−630	64−320	108
Co/SiO_2 (20% wt)	29	483	100−1100	300−420	106
Ni/SiO_2 (10% wt)	8	573	200−440	320−820	5

[a] Estimated using the regressed values of relevant parameters (Ru, Table 1; Co and Ni, Table S2).

represents an intrinsic metric of CH_4 selectivity for CO_2−H_2 reactions on any given catalyst and depends on reaction temperature and the mean diameter of metal nanoparticles.[3] The data shown in Figure 5 include two Ru catalysts with different mean nanoparticle diameters ($\langle d_p \rangle$, 2 and 3 nm) and evaluated at different temperatures (573 and 483 K); they showed very different $\gamma/(\alpha\beta)$ values (4 $kPa^{-0.5}$ for 2 nm, 573 K; 108 $kPa^{-0.5}$ for 3 nm, 483 K; Table 2). Smaller $\gamma/(\alpha\beta)$ values would give larger P_{CO}^{SS} values at any given CO_2 and H_2 pressures (eqs 11 and 14). The addition of CO at the P_{CO}^{SS} level determined from eqs 11 and 14 allows all Ru catalysts, irrespective of their intrinsic selectivities, to form exclusively CH_4 without any net CO formation (Figure 5).

3.2.3. CO Addition Strategies on Co and Ni Catalysts. CO addition strategies on Ru-based catalysts are rooted in the intermediate role of CO and the stronger CO inhibition of CO_2 conversion compared to CH_4 formation reactions. This sequential formation of CO and CH_4 from CO_2−H_2 reactants is also evident on dispersed Ni[8−11,16] and Co[5−7,33] nanoparticles, for which CO forms via direct CO_2 dissociation steps and CH_4 forms via subsequent CO hydrogenation mediated by H-assisted CO activation kinetically relevant steps.[9,16,33] DFT-derived energies[43,44] and transient spectroscopic studies[16,33] indicate that direct CO_2 dissociation to CO* (and O*) proceeds with lower activation barriers than H-assisted CO_2 activation routes (leading to formates or carboxylates) on Co and Ni, consistent with direct CO_2 dissociation as the predominant route to CO (and H_2O) on these catalysts and with the pathway on Ru nanoparticles (Scheme 1). Consequently, these mechanistic similarities render CO addition strategies also effective for selectivity control in CO_2−H_2 reactions on dispersed Co and Ni nanoparticles. This is demonstrated by the excellent agreement between measured outlet CO pressures and their respective predicted P_{CO}^{SS} values (Figure 5; P_{CO}^{SS} derivations, Section S3) on Co/SiO_2 (20% wt; $\langle d_p \rangle$ = 29 nm; 483 K; η_{RWGS} < 0.01) and Ni/SiO_2 (10% wt; 8 nm; 573 K; $\eta_{RWGS} \leq 0.1$) catalysts throughout broad ranges of temperature (483−573 K) and reactant pressures (100−1100 kPa CO_2, 300−820 kPa H_2). These Co and Ni catalysts showed intrinsic selectivity parameters ($\gamma/(\alpha\beta)$) similar to those of Ru at a given temperature (Table 2). Their CO_2 conversion and CH_4 formation rates are accurately described by the same rate equations (eqs 1 and 2) used for Ru-based catalysts (parity plots, Figure S1), thus making the same CO addition strategy effective for selectivity control on all three metals. These results confirm the general usefulness of the proposed CO addition strategy and its relevance for dispersed Ru, Co, and Ni nanoparticles at all temperatures (483−573 K) and pressures (4−1100 kPa CO_2; 8−820 kPa H_2) examined.

The success of this strategy merely requires an intermediate role of CO in CO_2−CO−CH_4 reaction sequences and CO inhibition effects that are stronger for CO_2 conversion (to CO) than CH_4 formation (from CO). These requirements are met for the range of catalysts and conditions examined in this study, which encompass the most competent CO_2 conversion catalysts and the pressures and temperatures relevant to the practice of these reactions.

3.2.4. CO Addition Strategies at Conditions that Lead to CO_2 Conversion Near RWGS Equilibrium. CO_2 conversion to CO (via RWGS; Scheme 1) ultimately approaches thermodynamic equilibrium values as CO_2 and H_2 reactants are consumed and H_2O is formed in RWGS and CO conversion to CH_4 along the bed, leading to rates described as

$$r_{CO2}^{net} = \frac{\alpha P_{CO2}\sqrt{P_{H2}}}{P_{CO}(1 + \beta P_{CO} + \delta\sqrt{P_{H2}} + \sigma P_{CO2}\sqrt{P_{H2}})} \cdot (1 - \eta_{RWGS}) \tag{15}$$

where η_{RWGS} denotes the RWGS approach to equilibrium (eq 5). The asymptotic form of eq 15 for surfaces at near-saturation CO* coverages (βP_{CO} as the predominant denominator term in eq 15) then becomes

$$r_{CO2}^{net} = \frac{\alpha P_{CO2}\sqrt{P_{H2}}}{\beta (P_{CO})^2} \cdot (1 - \eta_{RWGS}) \tag{16}$$

This expression, together with eq 7 for CH_4 formation, gives the value of P_{CO}^{SS} that varies as the RWGS approaches equilibrium:

$$P_{CO}^{SS} = \frac{K_{RWGS} P_{CO2} P_{H2}}{P_{H2O} + \frac{\gamma}{\alpha\beta} K_{RWGS} {P_{H2}}^{1.5}} \tag{17}$$

Equation 17 reduces to eq 11 for RWGS reactions far from equilibrium ($P_{H2O} \ll \frac{\gamma}{\alpha\beta} K_{RWGS} {P_{H2}}^{1.5}$). These P_{CO}^{SS} values (eq 17) decrease as H_2O forms and net RWGS rates (eq 16) decrease as CO_2 and H_2 are consumed and η_{RWGS} approaches unity along the bed. Such P_{CO}^{SS} trends with CO_2 and H_2 conversion indicate that all CO molecules, whether added at the inlet or formed indigenously from CO_2−H_2 reactants along the bed, ultimately form CH_4, the thermodynamic and kinetic endpoint of CO_2−CO−CH_4 reaction sequences, at sufficiently long bed residence times (simulation results shown in Section S4).

3.2.5. Implications of CO Addition Strategies: Selectivity Control without Requiring Complex Catalyst Architectures or Synthesis Protocols. The success of these CO addition strategies shows that complex synthesis protocols or catalyst architectures, which are unlikely to persist during extended use at relevant conditions or after periodic regenerations, are not required to tailor selectivity or form only CH_4 from CO_2−H_2 reactants. CO addition strategies enable the exclusive formation of CH_4 from CO_2−H_2 reactants, irrespective of reaction conditions (temperature, CO_2−H_2 pressures) or the composition, size, or structure of the catalytic metal nanoparticles. These strategies merely require that CO acts as an intermediate in sequential CO_2−CO−CH_4 reaction pathways and that the effects of CO inhibition are stronger for CO formation than for its consumption. Such strategies are thus expected to apply generally to any catalytic systems and CO_2−H_2 reaction pathways that satisfy these criteria, for which the requisite inlet CO pressure can be obtained by equating r_{CO2} and r_{CH4}, following the derivations presented in Sections 3.2.1 and 3.2.2. These selectivity control strategies are also relevant for the formation of higher hydrocarbons (C_xH_y) from CO_2 and H_2, which occurs through sequential CO_2−CO-C_xH_y reactions and shows weaker CO inhibition for C_xH_y formation via Fischer−Tropsch synthesis than for CO_2 conversion to CO.[12,34,35]

In practice, CO concentration gradients can develop not only axially along the bed, as discussed in Sections 3.1 and 3.2, but also radially within catalyst aggregates because of diffusional requirements that cannot be met under conditions of relevant practice. These aggregate-scale CO gradients are discussed in the next section; they can be rigorously described by using diffusion-reaction formalisms that are mathematically

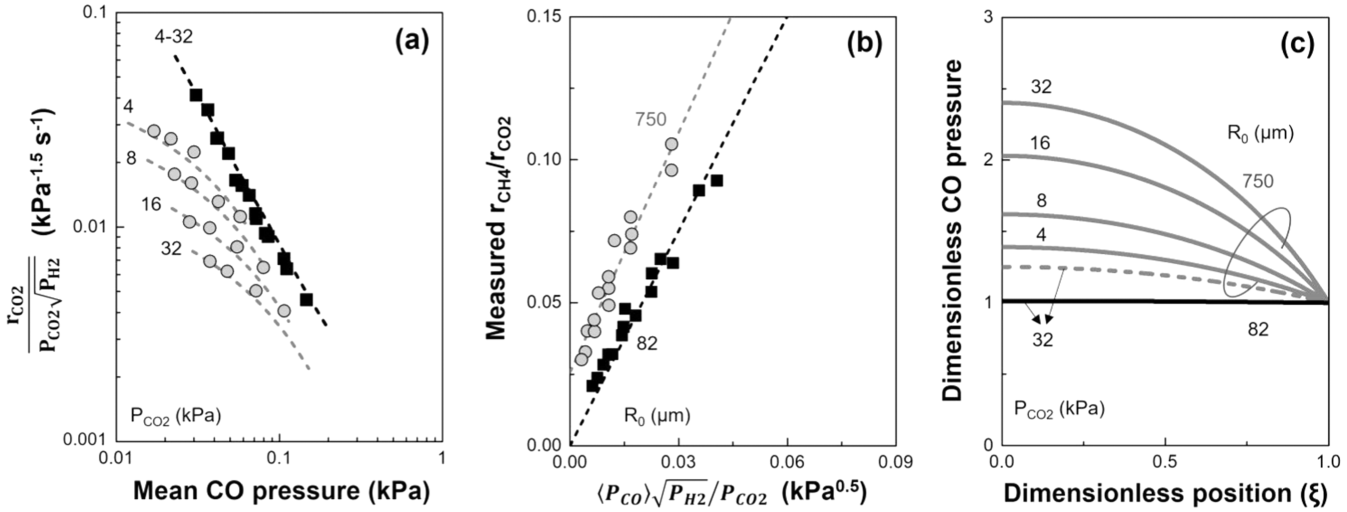

Figure 6. (a) Measured $r_{CO2}/(P_{CO2}\sqrt{P_{H2}})$ (eq 9) values with mean CO pressures on small (squares; R_0 = 82 μm; data from Figure 3, shown here for comparison) and large (circles; 750 μm) aggregates of 0.6% wt Ru/SiO$_2$ ($\langle d_p\rangle$=2 nm; 4−32 kPa CO$_2$, 8 kPa H$_2$, 573 K). Line: convection-reaction model predictions (eqs 3 and 4 with eqs 6 and 7). Curves: diffusion-convection-reaction model predictions (eqs 18−20 with eqs 6 and 7). (b) Measured CH$_4$ selectivities at different $\langle P_{CO}\rangle\sqrt{P_{H2}}/P_{CO2}$ pressure ratios on small (squares) and large (circles) aggregates. Dashed lines denote linear regressions. (c) Intra-aggregate P_{CO} profiles (relative to boundary values) calculated from diffusion-convection-reaction models for small and large aggregates at boundary CO pressures of 0.075 kPa (solid curves) and 0.21 kPa (dashed curve).

analogous to the convection-reaction mole balances for bed-scale CO gradients (eq 8). These similarities render CO addition strategies also relevant for controlling CO gradients within aggregates and ultimately CH$_4$ selectivities in catalysts affected by CO gradients at both the bed and aggregate scales, conditions that emerge ubiquitously in practical applications.

3.3. Intra-Aggregate CO Concentration Gradients and Consequences for Reactivity and Selectivity.

3.3.1. Descriptions of Rates and Selectivities in the Presence of Intra-Aggregate CO Gradients. Intra-aggregate gradients are most evident at low CO pressures because they lead to high CO formation rates (the "kernel" in eq 8) and to strong driving forces for the diffusional egress of CO from porous aggregates. This section describes how intra-aggregate CO gradients, which are most severe for the large aggregates required in practical packed-bed reactors, affect rates and selectivities and how they can be suppressed by the purposeful addition of CO to CO$_2$−H$_2$ reactants at levels prescribed by the mechanism-based rate equations reported in the previous sections.

Figure 6a shows $r_{CO2}/(P_{CO2}\sqrt{P_{H2}})$ values (eq 9) as a function of the prevalent mean CO pressure ($\langle P_{CO}\rangle$) at different inlet P_{CO2} values on 0.6% wt Ru/SiO$_2$ ($\langle d_p\rangle$ = 2 nm; 4−32 kPa CO$_2$, 8 kPa H$_2$; 573 K; $\eta_{RWGS} < 0.03$). The data on small aggregates (R_0 = 82 μm mean radius; squares) are well described by a single-valued function of P_{CO} at all CO$_2$ pressures, as discussed in Section 3.1 and as expected from the form of eq 9. These $r_{CO2}/(P_{CO2}\sqrt{P_{H2}})$ trends with CO pressures on small aggregates are accurately captured (dashed line, Figure 6a) by convection-reaction mole balances (eqs 3 and 4) using the relevant rate equations (eqs 6 and 7) and regressed parameters (0.6% wt Ru/SiO$_2$, Table 1). Measured CH$_4$ selectivities on the small aggregates show a single-valued linear dependence on $\langle P_{CO}\rangle\sqrt{P_{H2}}/P_{CO2}$ pressure ratios (squares, Figure 6b), consistent with the functional form of eq 10.

CO$_2$ conversion rates and the $r_{CO2}/(P_{CO2}\sqrt{P_{H2}})$ values on large aggregates (R_0 = 750 μm, circles, Figure 6a) are much smaller than on smaller aggregates for each given CO$_2$ and mean CO pressures; their deviations from convection-reaction model predictions (dashed line, Figure 6a) become more evident at lower mean CO pressures and higher CO$_2$ pressures (Figure 6a). Measured CO$_2$ conversion rates on large aggregates are no longer strictly proportional to CO$_2$ pressures, leading to additional CO$_2$ effects on $r_{CO2}/(P_{CO2}\sqrt{P_{H2}})$ values, which are absent on smaller aggregates (squares, Figure 6a) and unexpected based on the equations for r_{CO2} (eq 6). Measured CH$_4$ selectivities on large aggregates (circles, Figure 6b) are higher than those on small aggregates at any given $\langle P_{CO}\rangle$ values in the fluid phase; these selectivities remain nonzero even as $\langle P_{CO}\rangle$ (and $\langle P_{CO}\rangle\sqrt{P_{H2}}/P_{CO2}$) values approach zero. These results indicate that these fluid-phase $\langle P_{CO}\rangle$ values do not accurately represent the actual CO pressures "sensed" by the catalytic nanoparticles within larger aggregates; the CO concentrations within larger aggregates (but not within small aggregates) are in fact higher than those in the fluid phase, as shown by the diffusion-reaction mole balances described below.

Both intra-aggregate and interphase (between aggregate surface and adjacent fluid) temperature gradients are inconsequential for the large aggregates, as confirmed by the dimensionless diagnostic criterion for heat transfer effects in fixed-bed reactors established by Mears[45] and by heat flux analysis based on systematic dilution experiments[46] (details in Section S5). As a result, these "unexpected" discrepancies must reflect aggregate-scale radial concentration gradients in either reactants (CO$_2$, H$_2$) or products (CO, H$_2$O), which become more consequential at lower CO pressures and higher CO$_2$ pressures because they combine to give higher reaction rates. Accurate descriptions of such intra-aggregate radial concentration gradients and their consequences for rates (r_{CO2}, eq 6) and selectivities (r_{CH4}/r_{CO2}, eq 10) require diffusion-convection-reaction mole balances that account for gradients at both the bed and aggregate length scales.

Weisz−Prater criterion[47] estimates (Section S5) indicate that intra-aggregate CO$_2$ or H$_2$ concentration gradients cannot account for the rates and kinetic trends observed on large

Scheme 2. Schematic Depiction of the Dimensionless Diffusion-Convection-Reaction Model for CO Concentration Gradients along the Bed and within Catalyst Aggregates

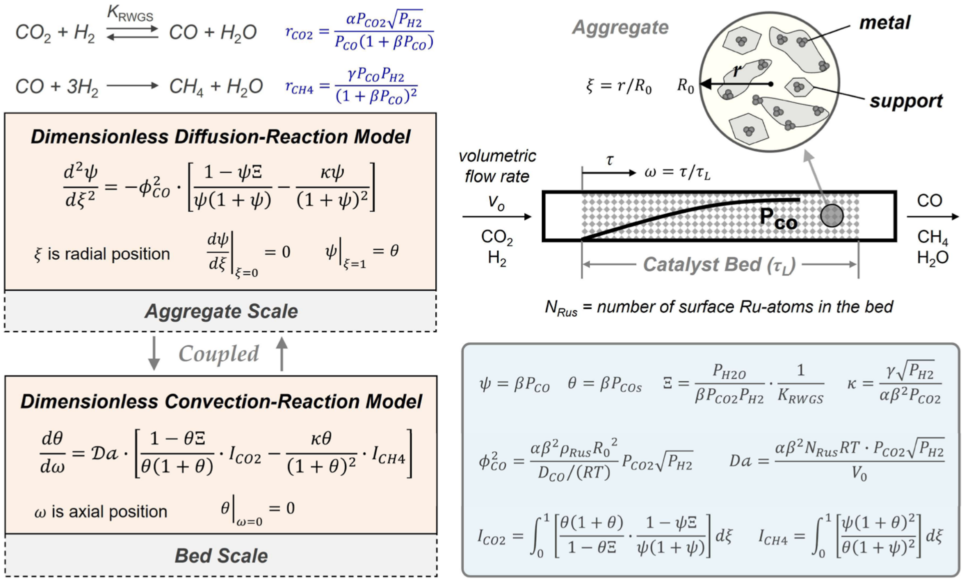

aggregates (Figure 6a). Radial H_2O concentration gradients, leading to intra-aggregate P_{H2O} values larger than in the fluid phase, would inhibit CO_2 conversion rates (eq 6) through thermodynamic constraints (η_{RWGS}, eq 5). This, in turn, would decrease local CO concentrations and lower CH_4 selectivities (as CO_2 conversion rates are more strongly inhibited by CO than CH_4 formation rates), in contradiction to the higher r_{CH4}/r_{CO2} ratios observed on the larger aggregates (Figure 6b).

The intermediate role of CO and its strong inhibition effects would cause rates to be affected by any prevalent radial CO gradients, as also observed in the case of axial gradients (Section 3.1). Scheme 2 shows an illustrative depiction of CO gradients within catalyst aggregates (mean radius, R_0) and along the bed (residence time, τ_L), with eqs 6 and 7 as the relevant rate equations for CO_2 conversion and CH_4 formation, respectively. These CO gradients develop both radially and axially as CO forms (r_{CO2}) and reacts (r_{CH4}) at each point along the two dimensions. The diffusion-reaction mole balances that account for the intra-aggregate radial CO gradients and the convection-reaction analogue that describes bed-scale axial CO gradients are depicted in their respective dimensionless forms, with dimensionless parameters defined in Scheme 2. These two mole balances are coupled; they combine to determine the CO concentration gradients at both the bed and porous aggregate scales and their consequences for rates and selectivities.

CO gradients at the aggregate scale are described by the dimensionless differential CO mole balance (Scheme 2; eq 18), with ξ as the dimensionless radial position ($\xi = r/R_0$) within aggregates ($\xi = 0$ at the centerline) and ψ as the dimensionless CO pressure at each position ξ (defined in Scheme 2). The Ξ term is a lumped parameter that includes K_{RWGS} and H_2O, CO_2, and H_2 pressures, accounting for the RWGS approach to equilibrium at position ξ, and κ is another lumped parameter that contains α, β, γ, and the reactant pressures, as defined in Scheme 2. The term in square brackets accounts for the net CO formation rate at each position ξ, by analogy with the "kernel" in eq 8, which describes these values at each axial position. The parameter ϕ_{CO} is the Thiele modulus for CO; it reflects the ratio of characteristic times for diffusion and reaction within aggregates (eq 19):

$$\frac{d^2\psi}{d\xi^2} = -\phi_{CO}^2 \cdot \left[\frac{1-\psi\Xi}{\psi(1+\psi)} - \frac{\kappa\psi}{(1+\psi)^2}\right] \tag{18}$$

$$\phi_{CO}^2 = \frac{\alpha\beta^2 \rho_{Rus} {R_0}^2}{D_{CO}/(RT)} P_{CO2}\sqrt{P_{H2}} \tag{19}$$

where R is the gas constant, D_{CO} is the effective CO diffusivity within aggregates, ρ_{Rus} is the volumetric density of surface Ru atoms within each aggregate, and R_0 denotes the characteristic diffusion distance within aggregates (half the slab thickness or the radius of a quasi-spherical pellet; Scheme 2). An infinite slab geometry (of thickness $2R_0$) is used here, but other geometries (e.g., spherical) can be rigorously described from the results for slab models using a shape factor (V_p/S_p; V_p is the particle volume and S_p is its external surface area) instead of R_0 in defining ϕ_{CO}.[48,49] The ϕ_{CO} parameter (eq 19) determines the severity of radial CO concentration gradients, with larger ϕ_{CO} values leading to more severe gradients.

The boundary conditions at the aggregate-fluid interface for the diffusion-reaction mole balances (eq 18) evolve axially along the bed as conversion proceeds; the requisite mole balances in the fluid phase are given by the dimensionless convection-reaction equation at each axial position (Scheme 2):

$$\frac{d\theta}{d\omega} = \mathcal{Da} \cdot \left[\frac{1-\theta\Xi}{\theta(1+\theta)} \cdot I_{CO2} - \frac{\kappa\theta}{(1+\theta)^2} \cdot I_{CH4}\right] \tag{20}$$

Here, ω is the dimensionless axial position, θ is the dimensionless fluid-phase CO pressure at position ω ($\theta = \beta P_{COs}$, P_{COs} is the CO pressure at the aggregate-fluid interface), and $\mathcal{Da}$ is the Damköhler number (defined in Scheme 2). I_{CO2} and I_{CH4} (Scheme 2) are effectiveness factors that denote the ratios of rates in the presence of radial CO gradients to those when such gradients are negligible and CO concentrations equal those in the fluid phase throughout the aggregates. I_{CO2}

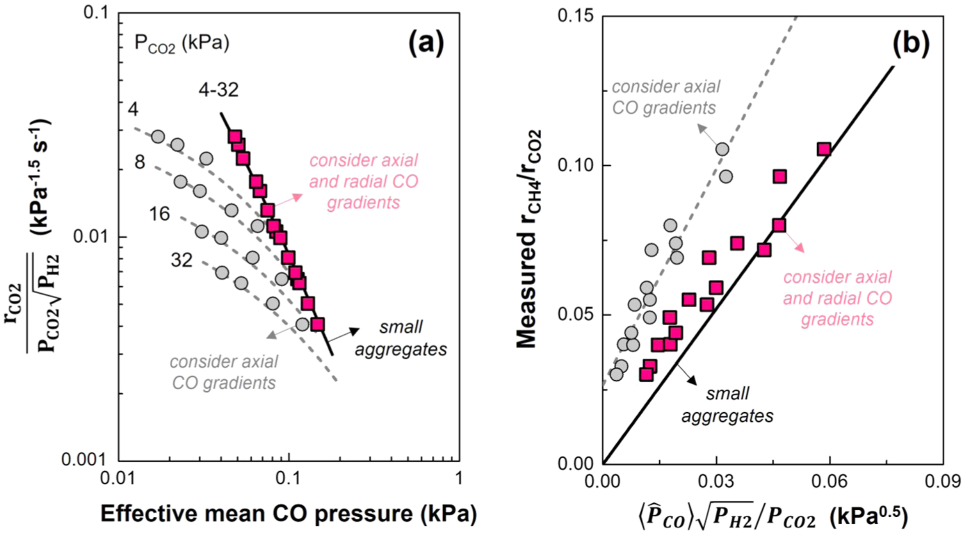

Figure 7. Measured (a) $r_{CO2}/P_{CO2}\sqrt{(P_{H2})}$ (eq 9) and (b) CH_4 selectivities with fluid-phase mean ($\langle P^f_{CO}\rangle$, eq 23; circles) and effective mean ($\langle\hat{P}_{CO}\rangle$, eqs 24 and 25; squares) CO pressures on the large aggregates of 0.6% wt Ru/SiO_2 ($\langle d_p\rangle$=2 nm; 4–32 kPa CO_2, 8 kPa H_2, 573 K). Dashed curves: diffusion-convection-reaction model predictions (eqs 18–20 with eqs 6 and 7); solid lines: data for small aggregates; dashed line: linear regression.

and I_{CH4} determine the consequences of intra-aggregate CO gradients for r_{CO2} and r_{CH4}, respectively.

The mole balances at the aggregate (eq 18) and bed (eq 20) scales are similar in the functional form of their respective "kernels" (terms in square brackets). CO concentration gradients reflect the combined effects of the two relevant dimensionless parameters (ϕ_{CO} for eq 18, $\mathcal{D}a$ for eq 20) and their respective "kernels" for each length scale. The inherent coupling between the aggregate- and bed-scale mole balances requires the simultaneous solution of these two equations (eqs 18 and 20) with boundary conditions for eq 18 given by

$$\left.\frac{d\psi}{d\xi}\right|_{\xi=0} = 0 \tag{21}$$

$$\psi|_{\xi=1} = \theta \tag{22}$$

which account for the symmetry at the aggregate centerline and for the CO pressure at the aggregate-fluid interface, set by the solution to the bed-scale equation (eq 20) at each axial position.

Measured $r_{CO2}/(P_{CO2}\sqrt{P_{H2}})$ values on large aggregates are accurately described by the diffusion-convection-reaction mole balances (dashed curves, Figure 6a; parity plots, Section S5) using the same kinetic parameters (α, β, γ, 0.6% wt Ru/SiO_2; Table 1) used to solve the convection-reaction equations for small aggregates, for which intra-aggregate CO gradients are negligible. The regressed ϕ_{CO} values range from 3 to 10 for CO_2 pressures between 4 and 32 kPa (8 kPa H_2, eq 19) for the data in Figure 6. These ϕ_{CO} values are similar to those estimated from eq 19 (6–22) using effective CO diffusivities (D_{CO}, 1.4×10^{-6} m^2 s^{-1}, 573 K) calculated from equivalent capillary diffusivities given by the Bosanquet equation (Knudsen number = 8) and tortuosity factors (1.5), the latter estimated from the void fraction of the aggregates (0.72) and diffusion simulations within porous structures consisting of random packings of quasi-spherical particles[50] (details in Section S5).

The magnitude of the dimensionless Thiele parameter (ϕ_{CO}, eq 19) and thus of the prevalent intra-aggregate CO gradients increases with CO_2 pressure for a given CO pressure at the aggregate-fluid interface (solid curves, Figure 6c). This leads to higher intra-aggregate mean CO pressures that differ most significantly from those in the fluid phase at large values of ϕ_{CO}, causing a concomitant decrease in r_{CO2} (eq 6) and $r_{CO2}/(P_{CO2}\sqrt{P_{H2}})$ values on larger aggregates (Figure 6a). The higher intra-aggregate CO pressures within larger aggregates also lead to higher CH_4 selectivities (Figure 6b) because of the stronger CO inhibition of CO_2 conversion than CH_4 formation (eq 10). These higher CH_4 selectivities reflect the strong radial CO gradients prevalent within larger porous aggregates instead of differences in intrinsic selectivity; the latter depends on the composition and structure of the dispersed metal nanoparticles, but not on the aggregate size for a given catalyst.

3.3.2. Effective Mean CO Pressures at Bed and Aggregate Scales for Rate and Selectivity Descriptions.

Catalyst aggregates are exposed to the fluid CO pressure at their axial position, but intra-aggregate gradients cause nanoparticles within porous aggregates to sense CO pressures exceeding those in the contacting fluid phase (Figure 6c). These effects render mean CO pressures ($\langle P_{CO}\rangle$), defined as the linear average of their values in the fluid phase between the inlet and outlet of the catalyst bed, inaccurate as a descriptor of rates and selectivities for large aggregates.

Large aggregates exhibit CO gradients both axially along the bed and radially within aggregates. The prevalence and significance of intra-aggregate gradients cause the rate and selectivity trends with linearly-averaged fluid-phase CO pressures ($\langle P_{CO}\rangle$) on large aggregates to deviate from those observed on smaller ones (Figure 6). These deviations become more evident as the Thiele parameter (ϕ_{CO}, eq 19) and the severity of intra-aggregate CO gradients increase (Figure 6a,b). Such deviations reflect the actual intra-aggregate CO pressures that nanoparticles sense; they cannot be resolved simply by using fluid-phase mean CO pressures ($\langle P^f_{CO}\rangle$; circles, Figure 7), calculated as

$$\langle P^f_{CO}\rangle = \int_0^1 P_{CO} d\omega \tag{23}$$

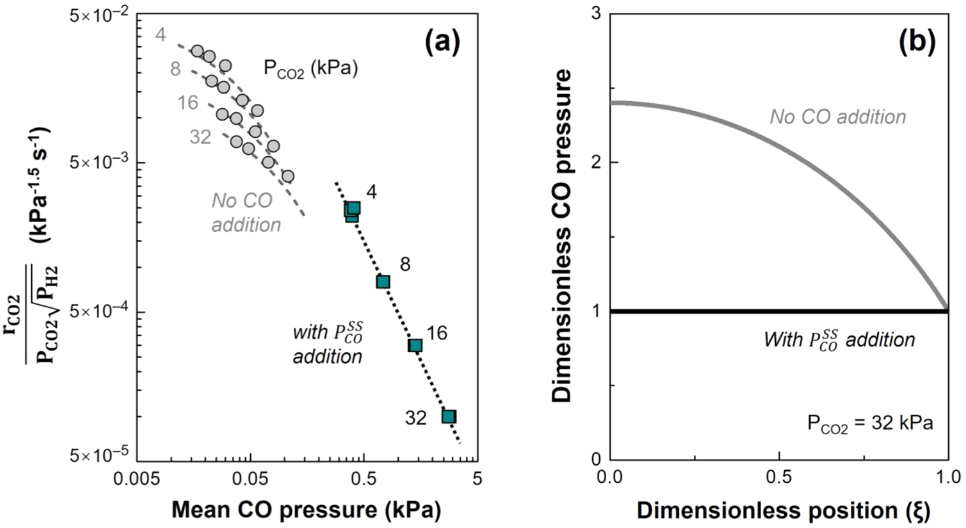

Figure 8. (a) $r_{CO2}/(P_{CO2}\sqrt{P_{H2}})$ (eq 9) values (squares) at different linearly-averaged mean CO pressures ($\langle P_{CO}\rangle$) for large aggregates of 0.6% wt Ru/SiO$_2$ ($\langle d_p\rangle$=2 nm; 4−32 kPa CO$_2$, 8 kPa H$_2$, 573 K) with P_{CO}^{SS} addition. Dashed line denotes the trend. Data from Figure 6a (circles) are displayed for comparison. (b) Intra-aggregate P_{CO} profiles (relative to boundary values) within large aggregates, calculated from diffusion-convection-reaction models (eqs 18−20, with eqs 6 and 7) at 32 kPa CO$_2$ with P_{CO}^{SS} addition. The P_{CO} profile without CO addition from Figure 6c (32 kPa CO$_2$, 750 μm) is displayed for comparison.

with P_{CO} as the fluid-phase CO pressure at each dimensionless axial position ω (Scheme 2) obtained from convection-reaction mole balances (eqs 3 and 4) that only account for the fluid-phase CO evolution along the bed. Resolving these deviations requires rigorous treatment of the radial CO concentration gradients within large aggregates.

Diffusion-convection-reaction mole balances (eqs 18−20) rigorously describe CO pressures at each position within aggregates and along the bed, thus enabling estimates of the effective mean CO pressures ($\langle\hat{P}_{CO}\rangle$) sensed by nanoparticles. These $\langle\hat{P}_{CO}\rangle$ values are given by

$$\langle\hat{P}_{CO}\rangle = \int_0^1\left(\int_0^1 P_{CO}d\xi\right)_{\omega} d\omega \tag{24}$$

for describing CH$_4$ selectivities (r_{CH4}/r_{CO2} proportional to P_{CO}, eq 10), and by

$$\frac{1}{\langle\hat{P}_{CO}\rangle\cdot(1+\beta\langle\hat{P}_{CO}\rangle)} = \int_0^1\left(\int_0^1 \frac{1}{P_{CO}(1+\beta P_{CO})}d\xi\right)_{\omega} d\omega \tag{25}$$

for describing $r_{CO2}/(P_{CO2}\sqrt{P_{H2}})$, which depends on $1/[P_{CO}(1+\beta P_{CO})]$ ratios (eq 9). Equations 24 and 25 rigorously account for CO gradients within aggregates (the inner integral across dimensionless radial position ξ at a given axial position ω) and along the bed (the outer integral across dimensionless axial position ω), as well as for the different dependencies of rates (eq 9) and selectivities (eq 10) on CO pressures. These $\langle\hat{P}_{CO}\rangle$ values effectively correct the inaccuracies of linearly-averaged mean CO pressures ($\langle P_{CO}\rangle$), which neglect both axial and radial CO gradients, and of fluid-phase mean CO pressures ($\langle P_{CO}^{f}\rangle$, eq 23), which neglect radial CO gradients within large aggregates. Using $\langle\hat{P}_{CO}\rangle$ to describe rates and selectivities on large aggregates (squares, Figure 7) eliminates their deviations from those observed on smaller ones (solid lines, Figure 7). These $\langle\hat{P}_{CO}\rangle$ values accurately represent the actual CO pressures sensed by nanoparticles dispersed along the bed and within aggregates; they deconvolute the influence of CO concentration gradients at both scales and recover the kinetic behaviors expected from the elementary steps (Scheme 1) and mechanism-based rate equations (eqs 6 and 7).

The observed CO$_2$ pressure effects on $r_{CO2}/(P_{CO2}\sqrt{P_{H2}})$ for large aggregates weaken as linearly-averaged ($\langle P_{CO}\rangle$, Figure 6a) and fluid-phase mean ($\langle P_{CO}^{f}\rangle$; eq 23; circles, Figure 7a) CO pressures increase; these $r_{CO2}/(P_{CO2}\sqrt{P_{H2}})$ values ultimately become similar at all CO$_2$ pressures and approach those observed on smaller aggregates (dashed curves, Figure 7a). These trends indicate that the effects of intra-aggregate CO gradients decrease as fluid-phase CO pressures increase; they reflect the decrease in the magnitude of the "kernel" in aggregate-scale mole balances (eq 18) as P_{CO} values at each radial position increase in response to the higher fluid-phase CO pressures, which set the boundary condition at the external surface of each aggregate (eq 22). This decreases, in turn, the net rate of CO formation at each radial position, thus weakening the intra-aggregate CO gradients for any given value of ϕ_{CO}. Such interpretations are confirmed by the diffusion-convection-reaction model (eqs 18−20), which predicts much weaker intra-aggregate CO gradients when the CO pressure at the aggregate-fluid boundary increases from 0.075 kPa (top solid curve, Figure 6c; 32 kPa CO$_2$) to 0.21 kPa (dashed curve, Figure 6c; 32 kPa CO$_2$). These data show how the magnitude of the "kernel" in eq 18, combined with the value of ϕ_{CO}, determines the severity of intra-aggregate CO gradients and their consequences for rates and selectivities. They also provide a compelling strategy for eliminating radial CO gradients within catalyst aggregates by tuning the boundary fluid-phase CO pressure to control the kernel, as discussed in the next section.

3.4. CO Addition Strategies for Eliminating CO Concentration Gradients at Both Aggregate and Bed Scales.

Section 3.2 describes a strategy to eliminate axial CO concentration gradients and form only CH$_4$ from CO$_2$−H$_2$ reactants, irrespective of catalyst composition or structure or the reaction conditions (temperature or pressure). The approach involved the addition of small amounts of CO at the bed inlet at pressures (P_{CO}^{SS}) prescribed by the functional form of the rate equations for CO_2 conversion (eq 1) and CH_4 formation (eq 2) and the regressed values of their rate parameters (Table 1). This CO pressure renders the rate of CO formation (from CO_2) equal to its rate of conversion (to CH_4) by making the value of the "kernel" in the axial CO mole balance (eq 8) equal to zero.

The functional forms of the "kernel" in the axial fluid-phase CO mole balance (eq 8) and in the aggregate-scale radial CO mole balance (eq 18) are identical; they both determine the net rate of CO formation at each point along their respective length scales. Such mathematical congruence implies that the CO pressure that eliminates CO gradients on one scale must also do so on the other scale. A zero value for the "kernel" in eq 18 sets $d^2\psi/d\xi^2$ to zero, which, along with the centerline symmetry condition (eq 21), renders ψ values equal to those in the fluid phase ($\psi = \theta$, eq 22) at all radial positions within aggregates. This, in turn, sets both effectiveness factors (I_{CO2} and I_{CH4}, Scheme 2) equal to unity, thus recovering the form of the axial CO mole balance for the case of negligible intra-aggregate CO gradients (eq 8). Consequently, the addition of CO at inlet pressures predicted from the mechanism-based equations for r_{CO2} and r_{CH4} (P_{CO}^{SS}) to the CO_2−H_2 reactants ($\eta_{RWGS} \ll 1$) simultaneously sets the "kernels" at both the bed and aggregate scales to zero, thereby eliminating CO gradients at all positions throughout both length scales.

These expectations were confirmed by measuring CO_2 conversion rates (4−32 kPa CO_2, 8 kPa H_2; 573 K; $\eta_{RWGS} <$ 0.03) on the large aggregates of 0.6% wt Ru/SiO_2 ($\langle d_p \rangle$ = 2 nm) with CO added at the inlet pressures predicted from eq 11 for each of the inlet CO_2 pressures (P_{CO}^{SS} = 0.4, 0.7, 1.4, and 2.8 kPa for P_{CO2} of 4, 8, 16, and 32 kPa, respectively) using the kinetic parameters regressed from the rate and selectivity data on smaller aggregates (Table 1). These measured $r_{CO2}/(P_{CO2}\sqrt{P_{H2}})$ values at different CO_2 pressures then become a single-valued function of the linearly-averaged mean CO pressure ($\langle P_{CO} \rangle$; squares, Figure 8a), as shown in Figure 8 and as expected from eq 9, the latter describing reaction rates in the absence of any intra-aggregate CO gradients. This is also evident from model-derived P_{CO} profiles within large aggregates, which show that CO concentrations remain equal to those at the aggregate-fluid boundary across all radial positions when the CO pressures in the fluid phase equal the model-derived P_{CO}^{SS} values (Figure 8b).

The addition of CO at these prescribed P_{CO}^{SS} inlet pressures was also examined at different bed residence times on large aggregates to demonstrate the simultaneous elimination of bed-scale axial CO gradients predicted by the model. The measured $r_{CO2}/(P_{CO2}\sqrt{P_{H2}})$ and P_{CO} values at each CO_2 pressure remained unchanged with bed residence time (superposed squares at each P_{CO2} value, Figure 8a). Moreover, P_{CO} values measured at different bed residence times are the same as those in the inlet stream and equal to the P_{CO}^{SS} values predicted by the rate equations (parity plot, Figure 5), confirming that the CO pressures remain constant across all axial positions along the bed of large aggregates. These data demonstrate that, in addition to the elimination of intra-aggregate CO gradients with P_{CO}^{SS} addition, axial CO gradients along the bed are also eliminated. Such P_{CO}^{SS} values set both the bed-scale (eq 8) and aggregate-scale (eq 18) "kernels" to zero, enforcing negligible net CO formation rates throughout the bed and aggregates and eliminating gradients at both scales; in doing so, the presence of CO at P_{CO}^{SS} levels in the inlet stream leads to the exclusive formation of CH_4, even for the large aggregates typically required in large-scale packed-bed reactors.

These CO addition strategies merely require an intermediate role of CO in CH_4 formation from CO_2−H_2 reactants and different effects of CO inhibition for CO_2 conversion (to CO) and CH_4 formation (from CO). The similar identity and kinetic relevance of elementary steps lead to rate equations similar in functional form for dispersed Ru, Co, and Ni nanoparticles. As a result, such strategies are effective for all three metals over a wide range of temperatures (483−573 K) and CO_2 and H_2 pressures (4−1100 kPa CO_2; 8−820 kPa H_2). The success of these strategies demonstrates how mechanistic insights into CO_2−H_2 turnovers and the mathematical treatments of rate and selectivity data using mechanism-based rate equations and coupled diffusion-convection-reaction constructs circumvent the need for catalysts with unique compositions, active sites, or architectures for selectivity control. In practice, the required inlet CO pressures are very small (Figure 5) and merely require the recycling of CO from effluent streams, thereby providing a practical strategy for the exclusive formation of CH_4 from CO_2−H_2 reactants, irrespective of catalyst intrinsic selectivity, reaction conditions (temperature, CO_2−H_2 pressures), or the composition and size of dispersed nanoparticles for Co, Ni, and Ru systems considered among the most competent metals for these reactions.

4. CONCLUSIONS

This study develops a mechanism-based strategy for controlling CH_4 and CO selectivities in CO_2−H_2 reactions on dispersed Ru, Co, and Ni nanoparticles, which are considered among the most competent metals for these reactions. This strategy involves the purposeful addition of small amounts of CO to CO_2−H_2 mixtures at the reactor inlet, with the required CO pressures accurately predicted by mechanism-based rate equations that are similar in functional form across Ru, Co, and Ni and embedded within diffusion-convection-reaction frameworks. Such CO addition strategies enforce negligible net CO formation rates along the catalyst bed and within porous aggregates, thus eliminating CO gradients at both scales and enabling the exclusive formation of CH_4 on all catalysts examined.

This strategy merely requires an intermediate role of CO in CH_4 formation from CO_2−H_2 reactants and different effects of CO inhibition for CO_2 conversion (to CO) and CH_4 formation (from CO). As a result, it is effective for all three metals examined over a wide and relevant range of temperature (483−573 K), CO_2 and H_2 pressures (4−1100 kPa CO_2; 8−820 kPa H_2), and nanoparticle diameter (2−30 nm), a consequence of the similar mechanisms and rate equations required to describe kinetic trends for CO formation and conversion on these catalysts. In practice, the small amounts of CO required can be readily recycled from the product streams, thereby providing a practical strategy that enables any catalyst composition (Ru, Co, Ni) or nanoparticle structure at any reaction condition to form CH_4 exclusively, without requiring specific catalytic compositions, architectures, or complex synthesis protocols, strategies that have, up to now, dominated the search for more active or selective catalysts for CO_2 conversion.

■ ASSOCIATED CONTENT

Supporting Information

The Supporting Information is available free of charge at https://pubs.acs.org/doi/10.1021/jacs.5c04698.

> Details of catalyst synthesis and characterization, derivations of CO_2 conversion and CH_4 formation rate equations, derivations of P_{CO}^{SS} for Co and Ni catalysts, simulation results at long bed residence times, diffusion coefficient estimations, Weisz−Prater criterion analysis, and heat transfer limitation analysis (PDF)

■ AUTHOR INFORMATION

Corresponding Author

Enrique Iglesia − *Department of Chemical and Biomolecular Engineering, University of California at Berkeley, Berkeley, California 94720, United States; Davidson School of Chemical Engineering, Purdue University, West Lafayette, Indiana 47907, United States;* orcid.org/0000-0003-4109-1001; Email: iglesia@berkeley.edu

Authors

Wenshuo Hu − *Department of Chemical and Biomolecular Engineering, University of California at Berkeley, Berkeley, California 94720, United States;* Present Address: Department of Chemical Engineering, Texas Tech University, Lubbock, Texas 79409, United States; orcid.org/0000-0001-8280-1167

Gregory L. Tate − *Department of Chemical and Biomolecular Engineering, University of California at Berkeley, Berkeley, California 94720, United States*

Complete contact information is available at: https://pubs.acs.org/10.1021/jacs.5c04698

Notes

The authors declare no competing financial interest.

■ ACKNOWLEDGMENTS

Financial support from Exxon Mobil Technology and Engineering Company is gratefully acknowledged. We also thank Francisco Villagra for his proofreading of the manuscript.

■ REFERENCES

(1) Zhou, C.; Asundi, A. S.; Goodman, E. D.; Hong, J.; Werghi, B.; Hoffman, A. S.; Nathan, S. S.; Bent, S. F.; Bare, S. R.; Cargnello, M. Steering CO_2 hydrogenation toward C-C coupling to hydrocarbons using porous organic polymer/metal interfaces. *Proc. Natl. Acad. Sci. U.S.A.* **2022**, *119* (7), No. e2114768119.

(2) Aitbekova, A.; Wu, L.; Wrasman, C. J.; Boubnov, A.; Hoffman, A. S.; Goodman, E. D.; Bare, S. R.; Cargnello, M. Low-Temperature Restructuring of CeO_2-Supported Ru Nanoparticles Determines Selectivity in CO_2 Catalytic Reduction. *J. Am. Chem. Soc.* **2018**, *140* (42), 13736−13745.

(3) Mansour, H.; Iglesia, E. Mechanistic Connections between CO_2 and CO Hydrogenation on Dispersed Ruthenium Nanoparticles. *J. Am. Chem. Soc.* **2021**, *143* (30), 11582−11594.

(4) Zhou, J.; Gao, Z.; Xiang, G.; Zhai, T.; Liu, Z.; Zhao, W.; Liang, X.; Wang, L. Interfacial compatibility critically controls Ru/TiO_2 metal-support interaction modes in CO_2 hydrogenation. *Nat. Commun.* **2022**, *13* (1), No. 327.

(5) Parastaev, A.; Muravev, V.; Huertas Osta, E.; van Hoof, A. J. F.; Kimpel, T. F.; Kosinov, N.; Hensen, E. J. M. Boosting CO_2 hydrogenation via size-dependent metal−support interactions in cobalt/ceria-based catalysts. *Nat. Catal.* **2020**, *3* (6), 526−533.

(6) Parastaev, A.; Muravev, V.; Osta, E. H.; Kimpel, T. F.; Simons, J. F. M.; van Hoof, A. J. F.; Uslamin, E.; Zhang, L.; Struijs, J. J. C.; Burueva, D. B.; Pokochueva, E. V.; Kovtunov, K. V.; Koptyug, I. V.; Villar-Garcia, I. J.; Escudero, C.; Altantzis, T.; Liu, P.; Béché, A.; Bals, S.; Kosinov, N.; Hensen, E. J. M. Breaking structure sensitivity in CO_2 hydrogenation by tuning metal−oxide interfaces in supported cobalt nanoparticles. *Nat. Catal.* **2022**, *5*, 1051−1060.

(7) Fan, T.; Liu, H.; Shao, S.; Gong, Y.; Li, G.; Tang, Z. Cobalt Catalysts Enable Selective Hydrogenation of CO_2 toward Diverse Products: Recent Progress and Perspective. *J. Phys. Chem. Lett.* **2021**, *12* (43), 10486−10496.

(8) Peng, G.; Sibener, S. J.; Schatz, G. C.; Ceyer, S. T.; Mavrikakis, M. CO_2 Hydrogenation to Formic Acid on Ni(111). *J. Phys. Chem. C* **2012**, *116* (4), 3001−3006.

(9) Vogt, C.; Groeneveld, E.; Kamsma, G.; Nachtegaal, M.; Lu, L.; Kiely, C. J.; Berben, P. H.; Meirer, F.; Weckhuysen, B. M. Unravelling structure sensitivity in CO_2 hydrogenation over nickel. *Nat. Catal.* **2018**, *1* (2), 127−134.

(10) Winter, L. R.; Gomez, E.; Yan, B.; Yao, S.; Chen, J. G. Tuning Ni-catalyzed CO_2 hydrogenation selectivity via Ni-ceria support interactions and Ni-Fe bimetallic formation. *Appl. Catal., B* **2018**, *224*, 442−450.

(11) van Herwijnen, T.; van Doesburg, H.; de Jong, W. A. Kinetics of the Methanation of CO and CO_2 on a Nickel Catalyst. *J. Catal.* **1973**, *28*, 391−402.

(12) Porosoff, M. D.; Yan, B.; Chen, J. G. Catalytic reduction of CO_2 by H_2 for synthesis of CO, methanol and hydrocarbons: challenges and opportunities. *Energy Environ. Sci.* **2016**, *9* (1), 62−73.

(13) National Academies of Sciences. *Engineering, and Medicine, Gaseous Carbon Waste Streams Utilization.*; The National Academies Press: Washington, DC, 2019.

(14) Kwak, J. H.; Kovarik, L.; Szanyi, J. CO_2 Reduction on Supported Ru/Al_2O_3 Catalysts: Cluster Size Dependence of Product Selectivity. *ACS Catal.* **2013**, *3* (11), 2449−2455.

(15) Wu, H. C.; Chang, Y. C.; Wu, J. H.; Lin, J. H.; Lin, I. K.; Chen, C. S. Methanation of CO_2 and reverse water gas shift reactions on Ni/SiO_2 catalysts: the influence of particle size on selectivity and reaction pathway. *Catal. Sci. Technol.* **2015**, *5* (8), 4154−4163.

(16) Simons, J. F. M.; de Heer, T. J.; van de Poll, R. C. J.; Muravev, V.; Kosinov, N.; Hensen, E. J. M. Structure Sensitivity of CO_2 Hydrogenation on Ni Revisited. *J. Am. Chem. Soc.* **2023**, *145* (37), 20289−20301.

(17) Wang, Y.; Winter, L. R.; Chen, J. G.; Yan, B. CO_2 hydrogenation over heterogeneous catalysts at atmospheric pressure: from electronic properties to product selectivity. *Green Chem.* **2021**, *23* (1), 249−267.

(18) Xin, H.; Lin, L.; Li, R.; Li, D.; Song, T.; Mu, R.; Fu, Q.; Bao, X. Overturning CO_2 Hydrogenation Selectivity with High Activity via Reaction-Induced Strong Metal-Support Interactions. *J. Am. Chem. Soc.* **2022**, *144* (11), 4874−4882.

(19) Zhang, W.; Lin, H.; Wei, Y.; Zhou, X.; An, Y.; Dai, Y.; Niu, Q.; Lin, T.; Zhong, L. Overturning CO_2 Hydrogenation Selectivity via Strong Metal−Support Interaction. *ACS Catal.* **2024**, *14* (4), 2409−2417.

(20) Kattel, S.; Liu, P.; Chen, J. G. Tuning Selectivity of CO_2 Hydrogenation Reactions at the Metal/Oxide Interface. *J. Am. Chem. Soc.* **2017**, *139* (29), 9739−9754.

(21) Li, X.; Lin, J.; Li, L.; Huang, Y.; Pan, X.; Collins, S. E.; Ren, Y.; Su, Y.; Kang, L.; Liu, X.; Zhou, Y.; Wang, H.; Wang, A.; Qiao, B.; Wang, X.; Zhang, T. Controlling CO_2 Hydrogenation Selectivity by Metal-Supported Electron Transfer. *Angew. Chem., Int. Ed.* **2020**, *59* (45), 19983−19989.

(22) Chen, M.; Li, B.; Wang, F.; Fang, J.; Li, K.; Zhang, C. Enhanced CH_4 Selectivity in CO_2 Hydrogenation on Bimetallic Pt−Ni Catalysts with Pt Nanoparticles Modified by Isolated Ni Atoms. *ACS Appl. Nano Mater.* **2023**, *6* (7), 5826−5834.

(23) Huang, Z.; Yuan, Y.; Song, M.; Hao, Z.; Xiao, J.; Cai, D.; Ibrahim, A. R.; Zhan, G. CO_2 hydrogenation over mesoporous Ni-Pt/

SiO_2 nanorod catalysts: Determining CH_4/CO selectivity by surface ratio of Ni/Pt. *Chem. Eng. Sci.* **2022**, *247*, No. 117106.

(24) Reddy, K. P.; Kim, D.; Hong, S.; Kim, K. J.; Ryoo, R.; Park, J. Y. Tuning CO_2 Hydrogenation Selectivity through Reaction-Driven Restructuring on Cu-Ni Bimetal Catalysts. *ACS Appl. Mater. Interfaces* **2023**, *15*, 9373−9381.

(25) Wei, C.; Ding, H.; Zhang, Z.; Lin, F.; Xu, Y.; Pan, W. Research progress of bimetallic catalysts for CO_2 hydrogenation to methane. *Int. J. Hydrogen Energy* **2024**, *58*, 872−891.

(26) Ray, K.; Deo, G. A potential descriptor for the CO_2 hydrogenation to CH_4 over Al_2O_3 supported Ni and Ni-based alloy catalysts. *Appl. Catal., B* **2017**, *218*, 525−537.

(27) Ye, R. P.; Ding, J.; Gong, W.; Argyle, M. D.; Zhong, Q.; Wang, Y.; Russell, C. K.; Xu, Z.; Russell, A. G.; Li, Q.; Fan, M.; Yao, Y. G. CO_2 hydrogenation to high-value products via heterogeneous catalysis. *Nat. Commun.* **2019**, *10* (1), No. 5698.

(28) Budi, C. S.; Wu, H. C.; Chen, C. S.; Saikia, D.; Kao, H. M. Ni Nanoparticles Supported on Cage-Type Mesoporous Silica for CO_2 Hydrogenation with High CH_4 Selectivity. *ChemSusChem* **2016**, *9* (17), 2326−2331.

(29) Das, S.; Perez-Ramirez, J.; Gong, J.; Dewangan, N.; Hidajat, K.; Gates, B. C.; Kawi, S. Core-shell structured catalysts for thermocatalytic, photocatalytic, and electrocatalytic conversion of CO_2. *Chem. Soc. Rev.* **2020**, *49* (10), 2937−3004.

(30) Wang, Y.; Arandiyan, H.; Scott, J.; Dai, H.; Amal, R. Hierarchically Porous Network-Like Ni/Co_3O_4: Noble Metal-Free Catalysts for Carbon Dioxide Methanation. *Adv. Sustainable Syst.* **2018**, *2* (3), No. 1700119.

(31) Dostagir, N. H. M. D.; Rattanawan, R.; Gao, M.; Ota, J.; Hasegawa, J.-y.; Asakura, K.; Fukouka, A.; Shrotri, A. Co Single Atoms in ZrO_2 with Inherent Oxygen Vacancies for Selective Hydrogenation of CO_2 to CO. *ACS Catal.* **2021**, *11* (15), 9450−9461.

(32) Hu, W.; Iglesia, E. Dynamics of Elementary Steps on Metal Surfaces at High Coverages: The Prevalence and Kinetic Competence of Contiguous Bare-Atom Ensembles. *J. Am. Chem. Soc.* **2024**, *146* (31), 22064−22076.

(33) Have, I. C. T.; Kromwijk, J. J. G.; Monai, M.; Ferri, D.; Sterk, E. B.; Meirer, F.; Weckhuysen, B. M. Uncovering the reaction mechanism behind CoO as active phase for CO_2 hydrogenation. *Nat. Commun.* **2022**, *13* (1), No. 324.

(34) Liu, J.; Hibbitts, D.; Iglesia, E. Dense CO Adlayers as Enablers of CO Hydrogenation Turnovers on Ru Surfaces. *J. Am. Chem. Soc.* **2017**, *139* (34), 11789−11802.

(35) Iglesia, E.; Hibbitts, D. The Fischer−Tropsch synthesis: A few enduring mechanistic conundrums revisited. *J. Catal.* **2022**, *405*, 614−625.

(36) Hibbitts, D.; Dybeck, E.; Lawlor, T.; Neurock, M.; Iglesia, E. Preferential activation of CO near hydrocarbon chains during Fischer−Tropsch synthesis on Ru. *J. Catal.* **2016**, *337*, 91−101.

(37) Yang, J.; Ma, W.; Chen, D.; Holmen, A.; Davis, B. H. Fischer−Tropsch synthesis: A review of the effect of CO conversion on methane selectivity. *Appl. Catal., A* **2014**, *470*, 250−260.

(38) Loveless, B. T.; Buda, C.; Neurock, M.; Iglesia, E. CO chemisorption and dissociation at high coverages during CO hydrogenation on Ru catalysts. *J. Am. Chem. Soc.* **2013**, *135* (16), 6107−6121.

(39) Weatherbee, G. D.; Bartholomew, C. H. Hydrogenation of CO_2 on Group-Viii Metals. 2. Kinetics and Mechanism of CO_2 Hydrogenation on Nickel. *J. Catal.* **1982**, *77* (2), 460−472.

(40) Weatherbee, G. D.; Bartholomew, C. H. Hydrogenation of CO_2 on Group-Viii Metals. 4. Specific Activities and Selectivities of Silica-Supported Co, Fe, and Ru. *J. Catal.* **1984**, *87* (2), 352−362.

(41) Bergeret, G.; Gallezot, P. *Handbook of Heterogeneous Catalysis*; Wiley-VCH Verlag GmbH & Co.: Weinheim, Germany, 2008.

(42) Avanesian, T.; Gusmão, G. S.; Christopher, P. Mechanism of CO_2 reduction by H_2 on Ru(0001) and general selectivity descriptors for late-transition metal catalysts. *J. Catal.* **2016**, *343*, 86−96.

(43) Dietz, L.; Piccinin, S.; Maestri, M. Mechanistic Insights into CO_2 Activation via Reverse Water−Gas Shift on Metal Surfaces. *J. Phys. Chem. C* **2015**, *119* (9), 4959−4966.

(44) Qi, Y.; Zhu, Y.-A.; Chen, D. Mechanism investigation and catalyst screening of high-temperature reverse water gas shift reaction. *Green Chem. Eng.* **2020**, *1* (2), 131−139.

(45) Mears, D. E. Diagnostic Criteria for Heat Transport Limitations in Fixed Bed Reactors. *J. Catal.* **1971**, *20* (2), 127−131.

(46) García-Diéguez, M.; Chin, Y.-H.; Iglesia, E. Catalytic reactions of dioxygen with ethane and methane on platinum clusters: Mechanistic connections, site requirements, and consequences of chemisorbed oxygen. *J. Catal.* **2012**, *285* (1), 260−272.

(47) Weisz, P. B.; Prater, C. D. Interpretation of Measurements in Experimental Catalysis. *Adv. Catal.* **1954**, *6*, 143−196.

(48) Hu, W.; Noh, G.; Iglesia, E. Consequences of metal-acid site proximity for alkane isomerization and β-scission mediated by bifunctional catalytic cascades. *J. Catal.* **2023**, *425*, 125−142.

(49) Aris, R. On Shape Factors for Irregular Particles. 1. The Steady State Problem-Diffusion and Reaction. *Chem. Eng. Sci.* **1957**, *6* (6), 262−268.

(50) Zalc, J. M.; Reyes, S. C.; Iglesia, E. The effects of diffusion mechanism and void structure on transport rates and tortuosity factors in complex porous structures. *Chem. Eng. Sci.* **2004**, *59* (14), 2947−2960.